Predicting the small-offset yield surfaces with polycrystal plasticity

Praveen Kumar[1†] and Sivasambu Mahesh[1*†]

[1]Department of Aerospace Engineering, Indian Institute of Technology Madras, Chennai, 600036, India.

*Corresponding author(s). E-mail(s): smahesh@iitm.ac.in;
Contributing authors: ae17d203@smail.iitm.ac.in;
†These authors contributed equally to this work.

Abstract

The small-offset yield surfaces of aluminium deformed in uniaxial tension, and free-end torsion to various finite strain levels are predicted using a binary tree based polycrystal plasticity model. The inelastic response of the model grains is taken to obey rate-independent plasticity, and anelasticity. The substructural state of each grain, comprised of dislocation densities, slip system hardness, backstress, and friction stresses are evolved during the deformation. Model parameters are algorithmically fitted to the measured yield surfaces of aluminium 1100 after uniaxial tensile deformation, as reported in the literature. With the same parameters, the model accurately captures the subsequent yield surfaces after free-end torsion also. Analysis of the model parameters reveals that coplanar interactions are mostly responsible for the sharp curvature at the nose of the yield surface. Also, anelastic strains, aided by backstress, are found to be essential to explain the large experimental Bauschinger effect.

Keywords: yield condition, crystal plasticity, polycrystalline material, numerical algorithms

1 Introduction

Yield surfaces of plastically deformed metallic materials have been objects of scientific interest for over a century. It has long been known that different definitions of yielding lead to qualitatively different yield surfaces [1]. On one hand, if yielding were associated with the departure of the stress-strain response from linearity [2, 3], the proportional yield surface is obtained. The proportional yield surface is also called the small-offset yield surface, as its practical determination necessitates a small excursion of the loading point into the inelastic regime, of the order of a few microstrain. On the other hand, the establishment of widespread plastic flow in the specimen occurs at a much larger plastic strain offset, which is commonly taken to be, 0.2% i.e., 2000 microstrain [4]. The corresponding yield surface is called the large-offset yield surface. The small-offset yield surface is typically highly distorted, with a considerably sharper curvature in the direction of prestraining than in the opposite direction. It does not enclose the origin in the stress space after even small prestrains [5–7]. The large-offset yield surface is considerably larger, and typically encloses the origin in the stress space [8]. Its elliptical shape can be explained on the basis of the crystallographic texture of the material [9]. Mair and Pugh [1] pointed out that the small-offset yield surface can find application in the study of plastic instabilities, while the large offset yield surface is relevant to the study of metal forming operations. The small-offset yield surface also finds application in modeling the spring-back of formed components, a subject of much recent interest [10, 11].

Numerous phenomenological models, recently reviewed by Yang et al. [12], have been proposed in the literature to predict the large-offset yield surfaces. In one often adopted approach, surveyed by Mánik [13], the yield condition is expressed in terms of a linear transformation of the stress tensor. A second approach involves incorporating a fourth order anisotropic tensor in the definition of the yield surface, as in Feigenbaum and Dafalias [14, 15]. A third approach, employed by Barlat et al. [16], Mánik et al. [17] and others, represents the microstructural state using a tensor variable and distorts the yield surface based on the deviation between the current deviatoric stress and the microstructural state tensors.

The literature on modeling the small-offset yield surface is considerably smaller. The phenomenological model of Pietryga et al. [18] aims to capture the evolution of the subsequent small-offset yield surfaces, and assumes a Hill-type yield surface. Their model incorporates isotropic, kinematic, and distortional hardening by embedding an evolving fourth-order tensor within the effective stress term. In another effort, Liu et al. [19] represented the polycrystalline aggregate as a single grain with 30 slip systems, which they termed slip components. They proposed a phenomenological hardening law with isotropic and kinematic parts, entailing self and latent hardening amongst the slip components. Recently, Aria et al. [20] reported full field elastoplastic crystal plasticity simulations to predict the yield surface of aluminium. The yield surfaces predicted in these works qualitatively match the shapes of the experimentally measured yield surfaces, but are not quantitatively comparable. The phenomenological model of Pietryga et al. [18] seeks to approximate the microstructural state of the material well enough to predict the mechanical response, by coarse-graining the microstructural behaviour to the scale of the material point. However, Liu et al. [19] and Aria et al. [20], based on polycrystal plasticity and full-field simulations, respectively, represent substructural evolution and the microstructural response at much finer scales.

Following the latter authors, the present work develops a model of substructure evolution, implements it within an existing polycrystal plasticity modeling framework, and uses it to predict subsequent small-offset yield surfaces. Existing polycrystal plasticity-based models [21–24] are able to predict the anisotropy in the mechanical response under load-reversal (Bauschinger effect), or load-crossing, all corresponding to large-offset strains. The present work, however, focuses on the small-offset regime. There are three essential differences between modeling the small-offset yield surfaces, and the large-offset mechanical response after strain-path changes: First, because the former probes over orders of magnitude smaller inelastic strains than the latter, it must account for deformation mechanisms that dominate at small inelastic strains ($\sim 10^{-5}$), but exhaust themselves at larger strains ($\sim\ 10^{-3}$). Second, obtaining accurate predictions in strain-path change tests requires capturing the mechanical response along only a few directions in the stress-space. However, predicting the small-offset yield surface calls for capturing the mechanical response along many more directions in the stress-space. In order to meet the latter objective a spatially realistic representation of the evolving substructure is required. Third, while the sub-structural state remains essentially constant during small-offset probing, it evolves appreciably during large-offset strain-path changes. It will be shown in the sequel that existing substructural models, developed in the context of modeling large-offset strain-path changes, are not adequate for predicting the small-offset yield surface.

The present work is structured as follows: The evolution of the model substructure during loading, which involves finite plastic strain, is described in Sec. 2. The numerical probing of the yield surface at constant substructural state reached after loading is then described in Sec. 3. After describing the algorithm for parameter fitting in Sec. 4, model predictions are compared with experimental measurements from the literature in Sec. 5. Insights about substructural interactions are then obtained from the fitted parametric values.

2 Loading

2.1 The binary tree model

The present model regards the material point of interest as a polycrystalline aggregate. The binary tree model regards the polycrystalline aggregate as a collection of sub-aggregates of varying sizes, interacting through the constraints of velocity and traction continuity across planar interfaces. The response of each sub-aggregate is obtained by volume averaging over its constituent sub-aggregates. The structure of these interactions are conceptually represented by the data structure called a binary tree [25].

A special case of the general binary tree, viz., a balanced binary tree is used to represent the polycrystal model presently. In the balanced binary tree model, the total number of grains is a power of 2. Individual grains, g, are associated with the lowest nodes in the binary tree, termed leaves. The leaf node of the binary tree that represents grain g is denoted (n_g). Higher nodes of the binary tree represent larger sub-aggregates of the polycrystalline aggregate, each comprised of all the nodes 'descended' from it. The top-most node, termed the root of the tree, and denoted (r), represents the entire polycrystalline aggregate.

A balanced binary tree representing a $2^3 = 8$ grain polycrystalline aggregate is depicted in Fig. 1. Nodes are arranged at different levels. The level of node (n) is denoted $\ell^{(n)}$; leaf nodes (n_g) have $\ell^{(n_g)} = 1$. Each node (n), except the leaf nodes, is connected to a pair of 'child' nodes denoted (l_n) and (r_n); these nodes are called 'siblings' of each other. Similarly, excepting the root node, each node (n) is also connected to a 'parent' node, (p_n). The number of nodes halves when marching up a level toward the root.

Sub-aggregates represented by the sibling nodes (l_n) and (r_n) are taken to be separated by a planar interface, normal to the unit vector $\boldsymbol{e}_2^{(n)}$. Let the mutually perpendicular unit vectors $\boldsymbol{e}_1^{(n)}$, and $\boldsymbol{e}_3^{(n)}$ be normal to $\boldsymbol{e}_2^{(n)}$, so that $\boldsymbol{e}_1^{(n)}$-$\boldsymbol{e}_2^{(n)}$-$\boldsymbol{e}_3^{(n)}$ form a right handed coordinate system. The necessary conditions for velocity, and traction continuity across the interface, expressed in component form in the $\boldsymbol{e}_1^{(n)}$-$\boldsymbol{e}_2^{(n)}$-$\boldsymbol{e}_3^{(n)}$ coordinate system, are [26, 27]:

$$\begin{aligned} &D_{11}^{(l_n)} = D_{11}^{(r_n)},\ D_{33}^{(l_n)} = D_{33}^{(r_n)},\ D_{13}^{(l_n)} = D_{13}^{(r_n)}, \\ &\sigma_{12}^{(l_n)} = \sigma_{12}^{(r_n)},\ \text{and}\ \sigma_{32}^{(l_n)} = \sigma_{32}^{(r_n)}, \end{aligned} \tag{1}$$

where $D_{ij}^{(n)}$ and $\sigma_{ij}^{(n)}$ denote the components of the rate of deformation tensor, and the deviatoric stress in node (n), respectively. $D_{ij}^{(n)}$ and $\sigma_{ij}^{(n)}$ are assumed to be uniform over the domain of the sub-aggregate represented by the node (n). Traction continuity normal to the interface takes the form

$$\sigma_{22}^{(l_n)} + p^{(l_n)} = \sigma_{22}^{(r_n)} + p^{(r_n)}, \tag{2}$$

where, $p^{(n)}$ denotes the hydrostatic pressure in node (n). Since it is possible to satisfy Eq. (2) for arbitrary $\sigma_{22}^{(l_n)}$, and $\sigma_{22}^{(r_n)}$, by selecting $p^{(l_n)}$, and $p^{(r_n)}$ appropriately, Eq. (2) represents but a trivial constraint on the $\sigma_{22}^{(n)}$-component of the deviatoric stresses.

Let the volume of grain g represented by the leaf node (n_g) be $V^{(n_g)}$. Then, the volume of the sub-aggregate represented by the node (n) is defined recursively as:

$$V^{(n)} = V^{(l(n))} + V^{(r(n))}. \tag{3}$$

Let the volume fractions of the left and right children of node (n) be denoted

$$\begin{aligned} \varrho^{(l_n)} &= V^{(l_n)}/V^{(n)},\ \text{and} \\ \varrho^{(r_n)} &= V^{(r_n)}/V^{(n)}. \end{aligned} \tag{4}$$

It is evident that $\varrho^{(l_n)} + \varrho^{(r_n)} = 1$.

The deformation rate, and the deviatoric stress in an arbitrary node, (n), are obtained by averaging over its children:

$$\begin{aligned} D_{ij}^{(n)} &= \varrho^{(l_n)} D_{ij}^{(l_n)} + \varrho^{(r_n)} D_{ij}^{(r_n)},\ \text{and} \\ \sigma_{ij}^{(n)} &= \varrho^{(l_n)} \sigma_{ij}^{(l_n)} + \varrho^{(r_n)} \sigma_{ij}^{(r_n)}. \end{aligned} \tag{5}$$

Let $\mathscr{N}^{(n)}$ be the set of all the descendants of node (n) that are leaves. Then, Eq. (5) can also be

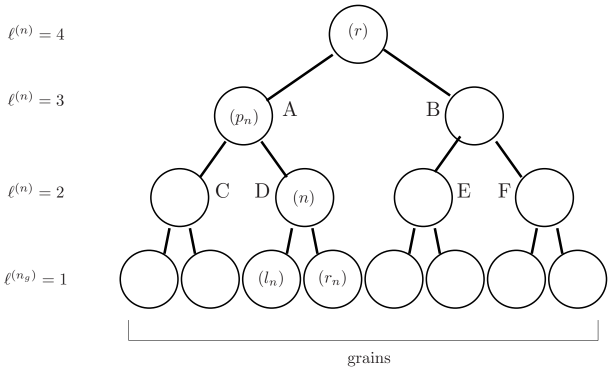

Fig. 1: A balanced binary tree model of an eight-grain polycrystal.

written as:

$$D^{(n)}_{ij} = \sum_{(n_g)\in\mathscr{N}^{(n)}} \frac{V^{(n_g)}}{V^{(n)}} D^{(n_g)}_{ij}, \text{ and}$$
$$\sigma^{(n)}_{ij} = \sum_{(n_g)\in\mathscr{N}^{(n)}} \frac{V^{(n_g)}}{V^{(n)}} \sigma^{(n_g)}_{ij}. \tag{6}$$

Let $L^{(n)}_{ij}$ denote the velocity gradient of node (n). Let $\boldsymbol{e}_1$-$\boldsymbol{e}_2$-$\boldsymbol{e}_3$ be a sample-fixed orthogonal coordinate system, and let

$$\mathscr{A} := \{11, 22, 33, 12, 21, 13, 31, 23, 32\}$$

be the set of all the components of 2-tensors in this coordinate system. Let the macroscopic velocity gradient components, $\bar{L}_{ij}$, where $ij \in \mathscr{L} \subseteq \mathscr{A}$ be imposed:

$$L^{(r)}_{ij} = \bar{L}_{ij}, \text{ for } ij \in \mathscr{L}. \tag{7}$$

Let $\mathscr{D}$ be the set of subscripts for which both $\bar{L}_{ij}$, and $\bar{L}_{ji}$ are imposed:

$$\mathscr{D} = \{ij : ij \in \mathscr{L}, \text{ and } ji \in \mathscr{L}\}, \tag{8}$$

and let

$$\bar{D}_{ij} = \frac{\bar{L}_{ij} + \bar{L}_{ji}}{2}, \text{ for } ij \in \mathscr{D}. \tag{9}$$

The components $ij \notin \mathscr{D}$ are said to be relaxed [28]. The macroscopic constraints imposed upon the root node, (r), are [27]:

$$D^{(r)}_{ij} = \bar{D}_{ij}, \text{ if } ij \in \mathscr{D}, \text{ and}$$
$$\sigma^{(r)}_{ij} = 0, \text{ if } ij \in \mathscr{A} \setminus \mathscr{D}. \tag{10}$$

In the present work, the $\boldsymbol{e}_1$-$\boldsymbol{e}_2$-$\boldsymbol{e}_3$ axes are taken to be directed along the axial, circumferential, and radial directions in the tubular specimens of Khan et al. [29], respectively. Uniaxial tension along x_1 corresponds to $\mathscr{D} = \{11\}$, and $\bar{D}_{11} = 1$. $\bar{\sigma}_{ij} = 0$, for $ij \notin \mathscr{D}$. Similarly, for loading in free-end torsion, $\mathscr{D} = \{12, 21\}$, and $\bar{D}_{12} = \bar{D}_{21} = 1$. $\bar{\sigma}_{ij} = 0$, for $ij \notin \mathscr{D}$. The imposed non-zero components of the velocity gradient are indicated schematically in Figs. 2a, and 2b for tension, and torsion, respectively.

2.2 The rate-independent plastic grain

Metallic grains deform elasto-plastically during loading. However, the elastic stretch is typically very small [30]. During loading to finite strains, plasticity is well-developed within the grains [31]. As considerable computational advantage can be gained by neglecting the elastic stretch in model grains undergoing well-developed plastic flow [32], model grains are taken to deform rigid-plastically.

Also, the present work is focused on yielding, which is realised microscopically by the activation of slip systems. In the rate-independent model of plastic slip [33], slip system activation unequivocally occurs at a definite resolved shear stress (RSS). This is in contrast to, e.g., the rate-sensitive viscoplastic model [34], wherein, any small non-zero RSS induces a non-zero slip rate.

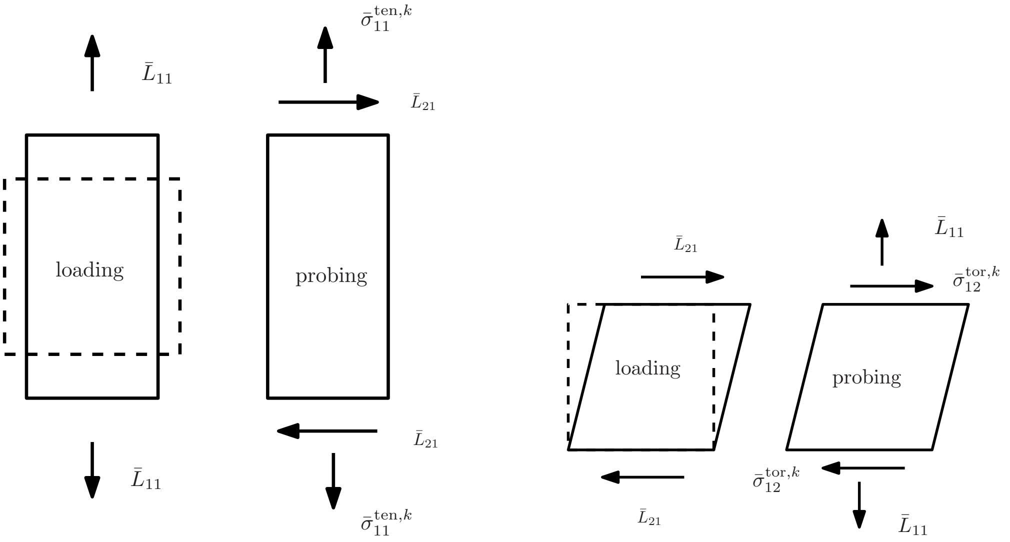

(a) Element deformation in uniaxial tension

(b) Element deformation in free-end torsion

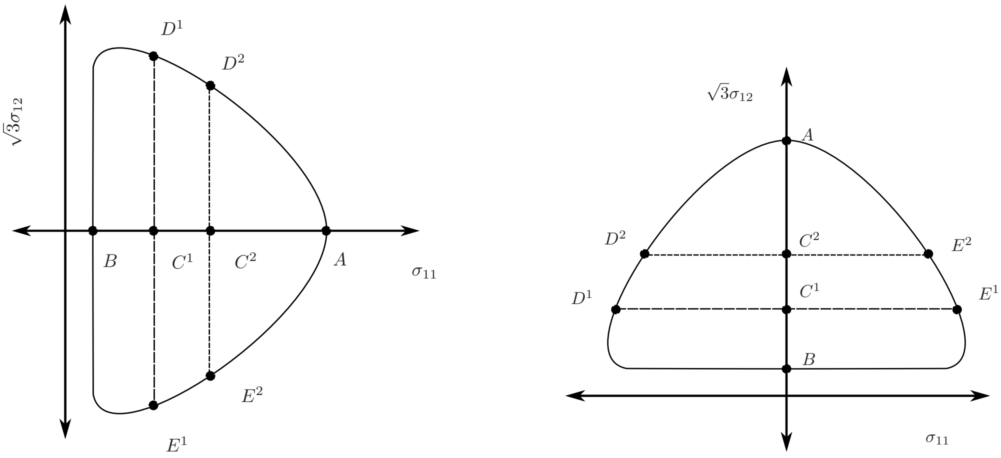

(c) Yield surface after tensile deformation

(d) Yield surface after torsional deformation

Fig. 2: Schematic deformation of a material point during loading and probing under (a) uniaxial tension, and (b) free-end torsion. The respective yield surfaces in the σ_{11}-$\sqrt{3}\sigma_{12}$ space are shown in (c) and (d).

To identify slip activation, a threshold slip-rate must then be prescribed. Rate-independent plasticity is presently preferred as it avoids the artifice of selecting a threshold slip-rate.

Each rigid-plastic and rate-independent grain, g, is assumed to accommodate the imposed deformation through rate-independent dislocation glide on slip systems $s \in \{1, 2, \ldots, S\}$. The unit slip direction, and slip plane normal of slip system (s) are denoted $\boldsymbol{b}^{(s),g}$ and $\boldsymbol{n}^{(s),g}$, respectively, which obey $\boldsymbol{b}^{(s),g} \perp \boldsymbol{n}^{(s),g}$. The non-negative slip-rate in slip system (s) is denoted $\dot{\gamma}^{(s),g}$. Slip systems with the same $\boldsymbol{n}^{(s),g}$, and positive and negative senses of $\boldsymbol{b}^{(s),g}$, or vice-versa, are treated as distinct slip systems.

The rate of deformation tensor of a grain is then given by [35]

$$D_{ij}^{(n_g)} = \sum_{s=1}^{S} m_{ij}^{(s),g} \dot{\gamma}^{(s),g}, \tag{11}$$

where the symmetric Schmid tensor is

$$m_{ij}^{(s),g} := \left(b_i^{(s),g} n_j^{(s),g} + n_i^{(s),g} b_j^{(s),g}\right)/2. \tag{12}$$

Slip systems (s) and (s') with $m_{ij}^{(s),g} = -m_{ij}^{(s'),g}$ are called reverse slip systems of each other.

Let $\tau^{(s),g}$ denote the critical resolved shear stress (CRSS) of slip system (s) in grain g. It is recalled that $\sigma_{ij}^{(n_g)}$ are the components of the deviatoric stress in it. The resolved shear stress (RSS) in slip system (s), $r^{(s),g}$ is then

$$r^{(s),g} = \sigma_{ij}^{(n_g)} m_{ij}^{(s),g}, \tag{13}$$

where summation over the repeated Latin indices is implied. Schmid's law [35] holds that

$$\dot{\gamma}^{(s),g} \begin{cases} = 0, & \text{if } r^{(s),g} < \tau^{(s),g}, \\ \geq 0, & \text{if } r^{(s),g} = \tau^{(s),g}. \end{cases} \tag{14}$$

In the rate-independent model, the case $r^{(s),g} > \tau^{(s),g}$ is unphysical, and the material response in that case is undefined.

Substituting Eq. (11) into first equation in Eq. (6),

$$D_{ij}^{(n)} = \sum_{(n_g)\in\mathscr{N}^{(n)}} \frac{V^{(n_g)}}{V^{(n)}} \sum_{s=1}^{S} m_{ij}^{(s),g} \dot{\gamma}^{(s),g}. \tag{15}$$

Using Eq. (15), the velocity continuity conditions across the sub-aggregate interfaces in Eq. (1) can be written as

$$\begin{aligned} \sum_{(n_g)\in\mathscr{N}^{(l_n)}} \frac{V^{(n_g)}}{V^{(l_n)}} \sum_{s=1}^{S} m_{ij}^{(s),g} \dot{\gamma}^{(s),g} = \\ \sum_{(n_g)\in\mathscr{N}^{(r_n)}} \frac{V^{(n_g)}}{V^{(r_n)}} \sum_{s=1}^{S} m_{ij}^{(s),g} \dot{\gamma}^{(s),g}, \end{aligned} \tag{16}$$

for $ij \in \{11, 33, 13\}$. Similarly, the imposed rate of macroscopic deformation in Eq. (10) can be written as

$$\sum_{(n_g)\in\mathscr{N}^{(r)}} \frac{V^{(n_g)}}{V^{(r)}} \sum_{s=1}^{S} m_{ij}^{(s),g} \dot{\gamma}^{(s),g} = \bar{D}_{ij}, \text{ if } ij \in \mathscr{D}. \tag{17}$$

Mahesh [27] showed that the problem of finding the slip rates, $\dot{\gamma}^{(s),g}$, in all the grains, and the deviatoric stress components $\sigma_{ij}^{(n)}$ in all the nodes can be expressed as the minimisation:

$$\min_{\dot{\gamma}^{(s),g}\geq 0} \sum_{(n_g)\in\mathscr{N}^{(r)}} V^{(n_g)} \tau^{(s),g} \dot{\gamma}^{(s),g}, \tag{18}$$

subject to the constraints given by Eqs. (16) and (17). In this minimisation problem, both the objective function, Eq. (18), and the constraints are linear in $\dot{\gamma}^{(s),g}$; it is thus a linear programming problem [36]. In the framework of linear programming, $\dot{\gamma}^{(s),g}$ represent the primal variables, and $\sigma_{ij}^{(n)}$ are found to be directly related to the dual variables. The solution of this problem satisfies Eqs. (1), (10), and Eq. (14). Physically, Eq. (18) expresses the condition of minimum internal plastic dissipation, which is equivalent to the principle of maximum external plastic dissipation [37]. The minimisation is presently performed using the efficient simplex algorithm [36], as implemented by the `GLPK` package [38].

With the slip rates, $\dot{\gamma}^{(s),g}$, determined in each grain, the plastic part of the velocity gradient of each leaf node, (n_g), is obtained as:

$$L_{ij}^{p,(n_g)} = \sum_{s=1}^{S} \dot{\gamma}^{(s),g} b_i^{(s),g} n_j^{(s),g}. \tag{19}$$

In analogy with Eq. (5), the plastic part of the velocity gradient in the higher nodes of the binary tree is obtained as:

$$L_{ij}^{p,(n)} = \varrho^{(l_n)} L_{ij}^{p,(l_n)} + \varrho^{(r_n)} L_{ij}^{p,(r_n)}. \tag{20}$$

For compatibility between sibling nodes, skew lattice spins, $W_{ij}^{p,(n)} = -W_{ji}^{p,(n)}$, must be superposed on each node of the binary tree:

$$L_{ij}^{(n)} = L_{ij}^{p,(n)} + W_{ij}^{p,(n)}. \tag{21}$$

A closed form expression for $W_{ij}^{p,(n)}$ may be found in Mahesh [26, 27, 39], and is not reproduced here. The lattice spins cause texture evolution during loading. At the root node, (r), Eq. (7) becomes:

$$L_{ij}^{(r)} = W_{ij}^{p,(r)} + L_{ij}^{p,(r)} = \bar{L}_{ij}, \text{ for } ij \in \mathscr{L}, \tag{22}$$

which can be solved to obtain the macroscopically imposed spin,

$$\begin{aligned} W_{ij}^{p,(r)} &= -W_{ji}^{p,(r)} \\ &= \begin{cases} 0, & \text{if } i = j, \\ \bar{L}_{ij} - L_{ij}^{p,(r)}, & \text{if } i \neq j, \text{ and } ij \in \mathscr{L}. \end{cases} \end{aligned} \tag{23}$$

2.3 Substructure

The model of substructure evolution given below is divided into the evolution of forest hardening, backstress, and friction stress, with plastic deformation. Forest hardening, and backstress contribute components $\tau_a^{(s),g}$, and $\tau_b^{(s),g}$, respectively, to the CRSS:

$$\tau^{(s),g} = \tau_a^{(s),g} + \tau_b^{(s),g}, \tag{24}$$

It is recalled that the CRSS determines the activation of slip system (s) through Schmid's law, Eq. (14). The friction stress, $\tau_c^{(s),g}$, determines the bowing or unbowing of pinned dislocation segments, and hence its anelastic response. It does not enter Schmid's law.

2.3.1 Forest hardening

Let $\rho^{(s),g}$ denote the forest dislocation density in slip system (s) in grain g. A storage-annihilation model of the dislocation density, due to Kocks [40], has been extended to individual slip systems by Rauch et al. [41]:

$$\dot{\rho}^{(s),g} = \frac{\dot{\gamma}^{(s),g}}{b\Lambda} - f\rho^{(s),g}\sum_{t=1}^{S}\dot{\gamma}^{(t),g}, \tag{25}$$

where b is the magnitude of the Burgers vector of the gliding dislocations, and K and f are fitting parameters that govern the rates of dislocation storage, and annihilation, respectively, and where the dislocation mean free-path Λ is given by:

$$\frac{1}{\Lambda} = \frac{\sqrt{\sum_{s=1}^{S}\rho^{(s),g}}}{K} + \frac{1}{D}, \tag{26}$$

where D is the grain diameter. In terms of the dislocation densities $\rho^{(s),g}$, the forest hardening contribution to the CRSS is given by the extended Taylor relation [42]

$$\tau_a^{(s),g} = \tau_{a0} + \mu b\sqrt{\sum_{t=1}^{S} a_{st}\rho^{(t),g}}, \tag{27}$$

where τ_{a0} denotes the CRSS in the absence of any substructure, μ the shear modulus, and a_{st} the dislocation interaction parameters. While there are, in principle, S^2 distinct a_{st}, crystallographic symmetries considerably reduce this number. In fcc grains deforming by $\{111\}\langle 110\rangle$ slip, although $S = 24$, there are only 6 distinct a_{st} corresponding to only 6 distinct types of interactions between pairs of slip systems. These interactions are self-hardening (SH), coplanar (Copl), cross-slip (CS), Hirth lock (HL) forming, glissile junction forming (GJ), and Lomer-Cottrell (LC) lock forming [42]. Kubin et al. [43] have determined the values of a_{st} for fcc crystals for typical values of the dislocation density through dislocation dynamics simulations. Their values for a_{st} are listed in Table 1, and adopted presently.

The notation for denoting the reverse slip system (s') of slip system (s) is recalled from Sec. 2.2. (s) and (s') are treated as distinct slip systems presently. $\tau_a^{(s),g}$ must be independent of their sense, positive or negative:

$$\tau_a^{(s),g} = \tau_a^{(s'),g}. \tag{28}$$

To enforce this physical condition, it is required that

$$a_{st} = a_{s't} = a_{st'} = a_{s't'}. \tag{29}$$

2.3.2 Backstress

The present model of backstress visualises the substructure as being divided into regions of low, and high dislocation density, as shown in Fig. 3a. These may be associated, e.g., with the cell interiors, and dense dislocation walls (DDW), respectively, as observed in plastically deformed aluminium [44]. Sessile dislocations in the DDW are modeled as a stacked pile-up [45, 46], with a highly localised internal stress field that decays exponentially over a length scale equal to the spacing of the stacked dislocations [47, Sec. 19.5]. Thus, dislocation segments approaching a DDW from the cell interior will experience a backstress,

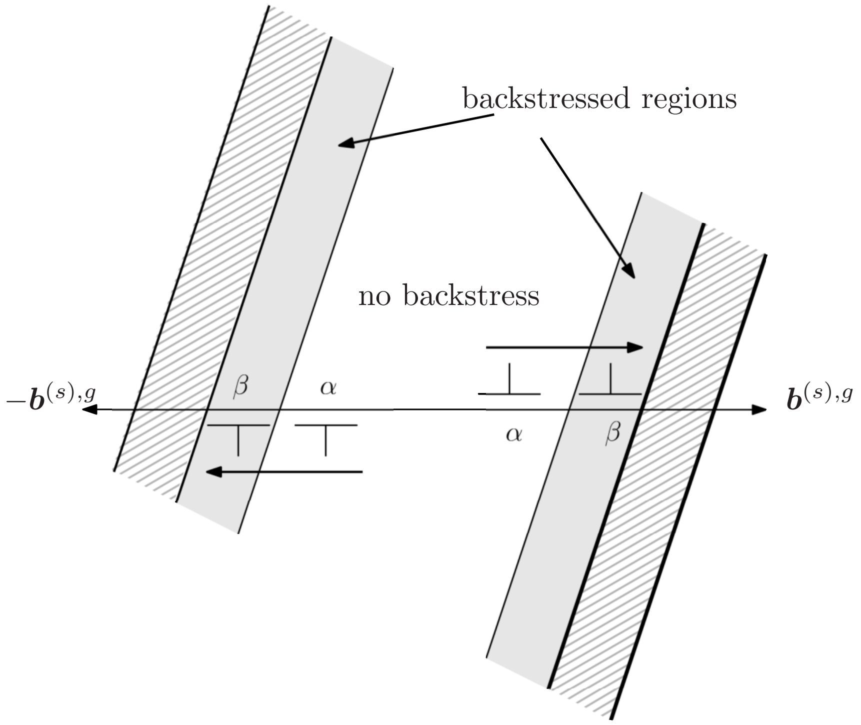

(a) Model of the substructure

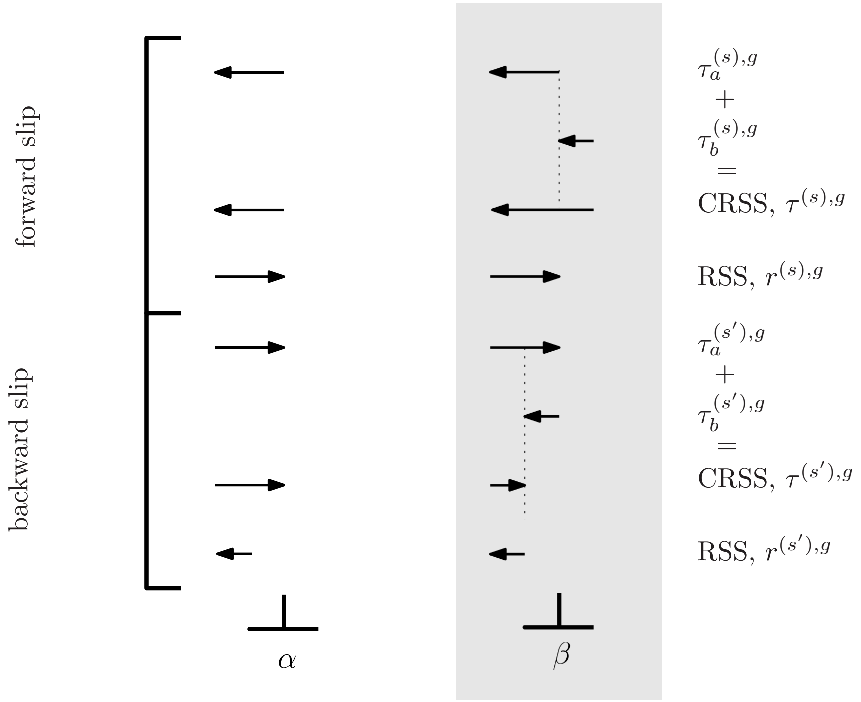

(b) CRSS constituents, and RSS

Fig. 3: (a) A schematic visualisation of the substructure underlying the backstress model. The hatched regions represent dislocation-rich regions, or DDW. The shaded region is the localised region of significant backstress. There is negligible backstress in the dislocation-poor cell interior. (b) RSS, and CRSS components on dislocations α, and β during forward and backward slip.

which is localised near the DDW, in the shaded region in Fig. 3a. The backstress is taken to be negligible outside the shaded region.

Consider two dislocation loops, α, and β, gliding in the same slip plane. At a certain instant, let loop α lie entirely within the cell interior and let the leading segments of loop β lie within the backstressed region, as shown schematically in Fig. 3a. Let the CRSS and RSS in this slip system be uniform, as shown in Fig. 3b. Loop α faces no backstress, while the leading segments of loop β experience backstress due to their proximity to the DDW.

First, consider the scenario depicted in the top half of Fig. 3b, labeled 'forward slip'. Suppose the applied RSS on the leading segments of loop α in the forward direction equals the CRSS, with a contribution from the forest hardening only. These segments will glide, and the loop will expand to produce slip. The leading segments of loop β experience the CRSS, with contributions from both forest hardening, and backstress. Thus, their glide is resisted by a larger CRSS than loop α. As the RSS on loops α and β are assumed equal, the leading segments of dislocation loop β will not glide. Thus, slip in the forward direction will be restricted to the backstress-free cell interior.

Next, consider the condition wherein the direction of the RSS is in the backward direction, so as to cause slip in (s'), as shown in the lower half of Fig. 3b. In this condition, the backstress counteracts the forest hardening, and thereby reduces the CRSS on loop β. If RSS equal to the CRSS were applied, loop β will contract. Under the same imposed RSS, loop α will not contract, unaided as it is by the backstress. Thus, dislocation glide in the reverse direction occurs only in the localised backstressed region near the DDW. As these simple considerations show, a localised region of backstress can cause yielding at a smaller applied stress in the reverse direction, than in the forward direction, i.e., a Bauschinger effect.

A model of backstress, due to Wen et al. [24], reduces to a simple form when applied to monotonic plastic deformation. It is now recalled in that form. Let $\rho^{(s),g}$ in Eq. (25) correspond to the reversible dislocation density in Wen et al. [24]. Let slip system (s) in grain g be activated during the monotonic deformation. According to Wen et al. [24], the backstress in slip system (s') is given by:

$$\tau_b^{(s'),g} = -\tau_a^{(s),g} f_B^s, \tag{30}$$

where, f_B^s is a fitting parameter. The simple proportionality between $\tau_b^{(s'),g}$, and $\tau_a^{(s),g}$ given by Eq. (30) was adequate to explain a number of experiments measuring the large-offset flow stress in Wen et al. [24]. It will be shown in the sequel that it is inadequate for the predicting the small-offset yield surfaces. This motivates its modification presently.

It is noted that Eq. (30) does not account for two physical features: (i) It assumes that backstress in (s') arises from dislocation pile-ups in slip system (s) only. Experimental studies [48, 49] have found that DDW are comprised of dislocations of all the slip systems that are activated during plastic deformation. A dislocation segment approaching a DDW will experience back-stresses not only from itself or its reverse slip system, but also from all the slip systems that contribute dislocations to the DDW. Also, the magnitude of the backstress will depend on the slip system of the approaching dislocation. (ii) The CRSS of slip system (s'), given by Eq. (24),

$$\begin{aligned} \tau^{(s'),g} &= \tau_a^{(s'),g} + \tau_b^{(s'),g} \\ &= \tau_a^{(s),g} + \tau_b^{(s'),g} \\ &= \tau_a^{(s),g} \left[1 - f_B^s\right], \end{aligned} \tag{31}$$

will become negative for $f_B^s > 1$, potentially triggering the plastic instability in the grain. The second equality in Eq. (31) follows from Eq. (28), and the third from Eq. (30). The present model addresses these two issues.

The backstress experienced by a dislocation segment near the DDW will depend upon the interaction between (i) the slip systems of the sessile stacked pile-up in the DDW, comprised of dislocations from all the activated slip systems [48, 49], and (ii) the slip system of the gliding forest dislocation. The structure of the dislocation interactions that affect the backstress resembles that underlying the a_{st} matrix of Sec. 2.3.1. This motivates the use of a similar matrix to capture the localised backstress developed. Paralleling a_{st} in Sec. 2.3.1, pairs of slip systems in the present fcc lattice are associated with 6 interaction coefficients:

$$b_{\mathrm{i}} \in \{b_{\mathrm{SH}}, b_{\mathrm{Copl}}, b_{\mathrm{CS}}, b_{\mathrm{GJ}}, b_{\mathrm{HL}}, b_{\mathrm{LC}}\}, \tag{32}$$

for the purpose of backstress computation. However, a key difference between hardening, and backstress is that the latter is sensitive to the direction of slip. Thus, (i) the coefficients, b_{i}, $\mathrm{i} \in \{\mathrm{SH}, \mathrm{Copl}, \ldots, \mathrm{LC}\}$ are signed material constants, and (ii) the interaction coefficient b_{st} between slip systems (s), and (t), and $b_{st'}$, between (s), and (t'), where (t') is the reverse slip system of (t) (Sec. 2.3.1) will generally be different: $b_{st} \neq b_{st'}$. However, reversing both s and t, $b_{st} = b_{s't'}$.

The Schmid tensors of slip systems (s), and (t) are recalled from Eq. (12). The value of b_{st} is taken to be

$$b_{st} = \begin{cases} 0, & \text{if } m_{ij}^{(s)} m_{ij}^{(t)} \geq 0, \text{and} \\ -b_{\mathrm{i}} m_{ij}^{(s)} m_{ij}^{(t)}, & \text{if } m_{ij}^{(s)} m_{ij}^{(t)} < 0. \end{cases} \tag{33}$$

The choice of i in Eq. (33) depends on the crystallographic relationship between slip systems (s), and (t). It must also be noted that the backstress induced by a slip system (s) on itself, $b_{ss} = 0$, according to Eq. (33). However, $b_{ss'} = -b_{\mathrm{SH}}/2$.

Let ρ^{ann} denote the dislocation density in the annealed material, and let the set $\mathscr{T}^g$ denote the set of slip systems with a sizable dislocation density:

$$\mathscr{T}^g = \{t : \rho^{(t),g} > \rho^{\mathrm{ann}}\} \subset \{1, 2, \ldots, S\}. \tag{34}$$

In analogy with Eq. (30), the backstress induced in slip system (s) may be taken as

$$\tau_b^{(s),g} = -\tau_a^{(s),g} \sum_{t \in \mathscr{T}^g} b_{st}. \tag{35}$$

This formulation will then suffer from the same deficiency as Eq. (31): Plastic instability may arise if $\sum_{t \in \mathscr{T}^g} b_{st} > 1$. Therefore, the form of the backstress is taken as:

$$\tau_b^{(s),g} = \begin{cases} -\tau_a^{(s),g} \left(1 - \exp\left[-\sum_{t \in \mathscr{T}^g} b_{st}\right]\right), & r^{(s),g} \leq 0, \\ 0, & r^{(s),g} > 0. \end{cases} \tag{36}$$

Thus, backstress are only accounted for in slip systems (s') that satisfy:

$$r^{(s'),g} \leq 0. \tag{37}$$

$\tau_a^{(s),g}$ in Eq. (36) is given by Eq. (27). Substituting Eq. (36) into Eq. (24), the CRSS is given by:

$$\tau^{(s),g} = \begin{cases} \tau_a^{(s),g} \exp\left[-\sum_{t \in \mathscr{T}^g} b_{st}\right], & \text{if } r^{(s),g} \leq 0 \\ \tau_a^{(s),g}, & \text{if } r^{(s),g} > 0. \end{cases} \tag{38}$$

It is interesting to note that the branches of the right side in Eq. (38) correspond to different physical locations in the idealised substructural model of Fig. 3: The first to the localised regions near DDW, and the second to the cell interiors. It is also evident from Eq. (38) that the CRSS in all slip systems remains positive for any b_{st}:

$$\tau^{(s),g} > 0. \tag{39}$$

This condition is sufficient to avoid instabilities during plastic deformation [35], and thus, essential for a general numerical implementation of the model. Finally, for small $\sum_{t \in \mathscr{T}^g} b_{st}$, Eq. (36) approaches Eq. (35), which in turn reduces to Eq. (30), due to Wen et al. [24], if all the b_{i} except b_{SH} were set to zero.

2.3.3 Friction stress

Inequality (39) implies that the direction of the applied stress must be reversed, as shown in Fig. 3b, in order to obtain the reverse yield point. However, in the experiments of Khan et al. [29], and in a number of other experimental studies, the reverse yield point has the same sign as the forward yield point. In other words, the material yields in reverse even before it is fully unloaded from the forward yield point. This suggests that another physical mechanism must be responsible for reverse yielding.

It is proposed that anelasticity, aided by backstress, is the physical mechanism underlying the early onset of reverse yielding. Anelastic deformation is caused by the bowing and unbowing of segments of existing dislocations pinned at hard pinning points [50]. This is in contrast to plastic deformation, which is characterised by the motion

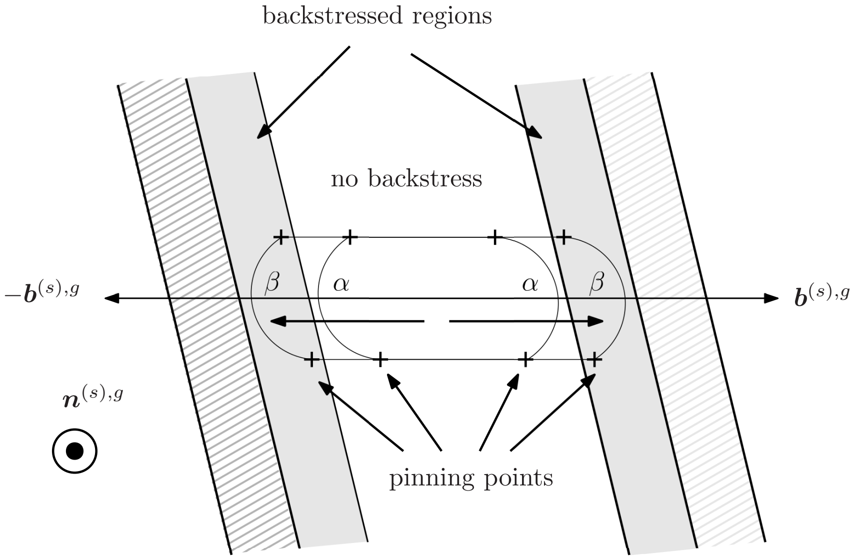

(a) Model of the substructure

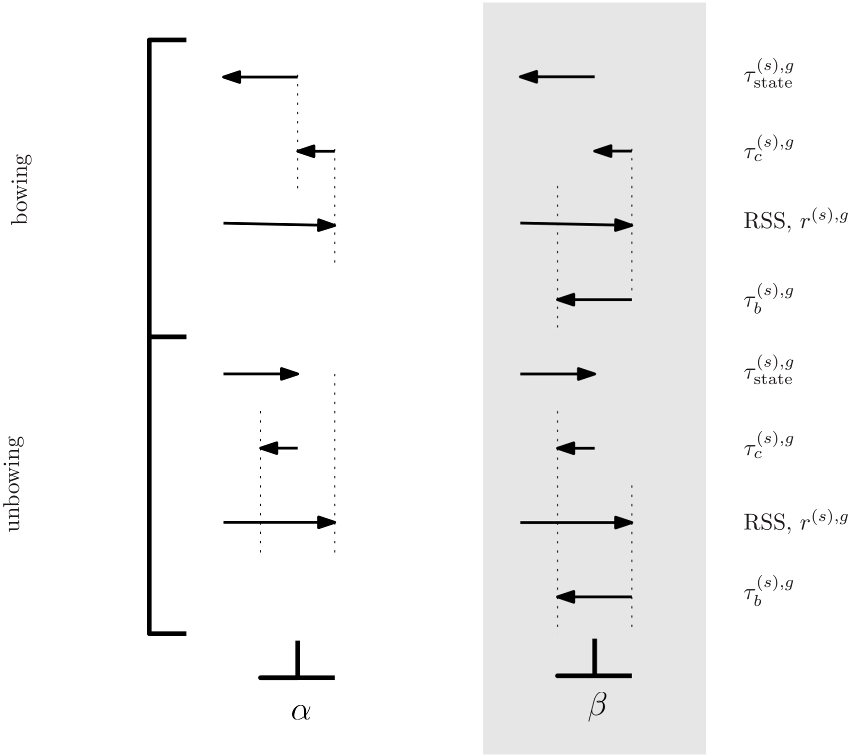

(b) CRSS, and effective RSS constituents

Fig. 4: (a) A schematic visualisation of the substructure and its influence on dislocation bowing and unbowing. The hatched, shaded, and clear regions have the same meanings as in Fig. 3. (b) Bowing state, RSS, backstress, and friction stress components on dislocations α, and β during inelastic dislocation bowing, and unbowing.

of dislocation segments surmounting obstacles, and dislocation multiplication.

The resistance to the bowing and unbowing of dislocations varies with the prestrain in the specimen. After a survey of several materials deformed in tension to various prestrains, Li and Wagoner [50] found that the applied stress at which anelastic deformation begins, termed the elastic-anelastic transition stress, depends non-monotonically on the prestrain. To account for the elastic-anelastic transition stress in their model, they introduced the notion of a friction stress: A necessary condition for anelastic deformation is that the applied stress must differ from the anelastic state by at least the friction stress. Although the term 'friction stress' usually refers to the lattice resistance in a defect-free lattice, in Li and Wagoner [50], this term also encompasses the drag experienced by bowing and unbowing dislocation segments due to weak obstacles in the form of dislocation debris. The term 'friction stress' is used in the latter sense presently.

The notion of a prestrain dependent friction stress is presently extended to the slip systems. Let $\tau_c^{(s),g}$ denote the friction stress in slip system (s) in grain g. In analogy with Eq. (27), the friction stress is taken to depend on dislocation density as

$$\tau_c^{(s),g} = \tau_{c0} + \mu b \sqrt{\sum_{t=1}^{S} c_{st} \rho^{(t),g}}, \tag{40}$$

where τ_{c0} denotes the friction stress of the defect-free lattice, and c_{st} denotes the interaction parameter between slip systems (s), and (t), obeying the crystallographic symmetries that underlie a_{st} in Eq. (27), viz., $c_{st} = c_{s't} = c_{st'} = c_{s't'}$. Paralleling Eq. (28), these conditions ensure that

$$\tau_c^{(s),g} = \tau_c^{(s'),g}. \tag{41}$$

The bowing state, $\tau_{\text{state}}^{(s),g}$, of the pinned dislocation segments in slip system (s), in grain g depends on both the prior history of RSS applied to the slip system, and the friction stress, $\tau_c^{(s),g}$. Following Li and Wagoner [50], a pinned dislocation segments is taken to bow further if

$$r_{\text{eff}}^{(s),g} \geq \tau_{\text{state}}^{(s),g} + \tau_c^{(s),g}, \tag{42}$$

where the effective RSS in the slip system is obtained by adding the backstress to the actual imposed RSS:

$$r_{\text{eff}}^{(s),g} = r^{(s),g} + \tau_b^{(s),g}. \tag{43}$$

After bowing, the bowing state increases to

$$\tau_{\text{state}}^{(s),g} = r_{\text{eff}}^{(s),g} - \tau_c^{(s),g}. \tag{44}$$

Similarly, pinned dislocation segments are taken to unbow if

$$r_{\text{eff}}^{(s),g} \leq \tau_{\text{state}}^{(s),g} - \tau_c^{(s),g}, \tag{45}$$

whereupon their bowing state decreases to

$$\tau_{\text{state}}^{(s),g} = r_{\text{eff}}^{(s),g} + \tau_c^{(s),g}. \tag{46}$$

The bowing of dislocation segments of slip system (s) is equivalent to their unbowing when described in terms of the reverse slip system (s'), and vice-versa. For consistency of the conditions given by Eqs. (42)–(46), it necessary that

$$\tau_{\text{state}}^{(s),g} = -\tau_{\text{state}}^{(s'),g}. \tag{47}$$

The dislocation loops of Fig. 3a are shown in the view looking down upon the slip plane in Fig. 4a. The leading segments of both the loops are shown in the same bowed state, $\tau_{\text{state}}^{(s),g} > 0$, say. The RSS, $r^{(s),g}$, required for incepting additional dislocation bowing in the cell interior, following Eq. (42) is shown in the top half of Fig. 4b, labeled 'bowing'. Let the same RSS be imposed in the near-DDW region also. There, the imposed RSS is counteracted by the backstress, $\tau_b^{(s),g}$, resulting in a smaller effective RSS, which is inadequate to incept bowing. Thus, when subjected to gradually increasing RSS, dislocation bowing in the cell interiors will precede that in the near-DDW backstressed regions.

Next, consider dislocation unbowing under gradually decreasing RSS, following Eq. (45). This condition is depicted in the lower half of Fig. 4b, labeled 'unbowing'. Counteracted by the backstress, $\tau_b^{(s),g}$, the effective RSS in the backstressed region is seen to satisfy Eq. (45), and thereby incept unbowing. Unaided by backstress, the RSS in the cell interior cannot incept unbowing. Thus, under decreasing RSS, unbowing in the back-stressed near-DDW regions precedes that in the cell interior.

In the initial annealed state, it is reasonable to assume that dislocations are not bowed, i.e., $\tau^{(s),g}_{\text{state}} = 0$. During plastic deformation accompanying loading, $\tau^{(s),g}_{\text{state}}$ is evolved according to Eq. (40), and Eqs. (44), or (46), following Li and Wagoner [50]. Besides plastic deformation, heat treatment, and stress relaxation steps also affect the state of the microstructure, and hence, $\tau^{(s),g}_{\text{state}}$. Hart and Solomon [59] observed that the mechanical response of plastically deformed Al specimen subjected to strain-hold experiments revealed a large but transient anelastic deformation component. If this anelastic deformation were associated with the unbowing of dislocation segments between pinning points, it would correspond to a reduction of $|\tau^{(s),g}_{\text{state}}|$.

3 Yield surface probing

The internal state of the substructure of each grain in the polycrystal model is established during loading. It is revealed during probing. Experimentally probing the yield surface requires small transgressions into the inelastic regime, whose effect on the substructural state is neglected in the model.

3.1 Plastic probing

After loading in either uniaxial tension, or free-end torsion, and holding the sample at constant strain for stress relaxation, Khan et al. [29] probed the yield surfaces, which are depicted schematically in Figs. 2c, and 2d. They found that the forward yield point in the direction of loading, labeled A in Figs. 2c, and 2d, coincided with the stress-relaxed loading point. They obtained the reverse yield point, labeled B, by decreasing the applied stress. Under the application of various stresses along the loading path, C^k, bounded by the forward and reverse yield points, they probed orthogonal to the direction of applied loading, and obtained the cross-directional yield stresses, D^k, and E^k. The computational simulation of the probing process is presently described.

It is physically reasonable and computationally advantageous to model unloading from the plastic loaded state assuming elastic material response [32]. During elastic unloading, the anisotropic stiffness of the grains will cause the build up of residual stresses. The stiffness matrix of the present Al grains, however, is nearly elastically isotropic [51]. Therefore, the residual stresses developed due to elastic incompatibility during unloading can also be neglected, and the model grains can be approximated as rigid plastic during yield surface probing. The error introduced by this assumption is bounded in Sec. 5.

The present assumption of elastic isotropy at the crystal level limits the present model to predicting the yield surfaces of nearly isotropic materials such as Al. In its present form, the probing scheme is not applicable to crystalline materials with greater elastic anisotropy, such as steel [52].

The binary tree model can also capture the onset of plasticity in the model polycrystal, i.e., the first activation of slip. If the continuity conditions in Eq. (1) were replaced by

$$\begin{aligned} &\sigma^{(l_n)}_{11} = \sigma^{(r_n)}_{11},\ \sigma^{(l_n)}_{33} = \sigma^{(r_n)}_{33},\ \sigma^{(l_n)}_{13} = \sigma^{(r_n)}_{13},\\ &\sigma^{(l_n)}_{12} = \sigma^{(r_n)}_{12},\ \text{and}\ \sigma^{(l_n)}_{32} = \sigma^{(r_n)}_{32}, \end{aligned} \tag{48}$$

the Sachs [53] iso-stress model is obtained. Imposing Eq. (10) at the root node, (r), and enforcing Eq. (48) between the sub-aggregates predicts the stress state at onset of yielding. Microstructurally, the onset of yielding corresponds to activation of the weakest slip system in the polycrystal [35]. Computationally, this problem can be solved as a linear program minimising Eq. (18) subject only to the constraints given by Eq. (17).

Imposing Eq. (10) determines the yield stresses along the forward and reverse directions of loading in Fig. 2c, and Fig. 2d. Determining the lateral faces requires imposing mixed conditions of the form:

$$\begin{aligned} D^{(r)}_{ij} &= \bar{D}_{ij},\ \text{if}\ ij \in \mathscr{D},\ \text{and}\\ \sigma^{(r)}_{ij} &= \bar{\sigma}_{ij},\ \text{if}\ ij \in \mathscr{A} \setminus \mathscr{D}, \end{aligned} \tag{49}$$

upon the root node, (r).

The predicted yield stress obtained by imposing Eq. (49) at the root node, (r), and Eq. (48) at all the sub-aggregate interfaces corresponds to the activation of slip in the weakest slip system(s). However, experimentally, Khan et al. [29] have associated yielding with a small, but non-zero inelastic strain of 10^{-5}. At the point of yielding in the experiment, a fraction of the grains in the polycrystal is expected to deform plastically through slip, while their neighbours maintain compatibility by deforming elastically [31]. In order to capture this physical feature of the deformation, the computational definition of yielding must be modified so that yielding is identified with slip activation in a fixed fraction of grains, and not in the weakest slip system of one grain only.

To this end, Eq. (49) is replaced with:

$$\begin{aligned} D_{ij}^{(n^{\mathrm{imp}})} &= \bar{D}_{ij}, \text{ if } ij \in \mathscr{D}, \text{ and} \\ \sigma_{ij}^{(n^{\mathrm{imp}})} &= \bar{\sigma}_{ij}, \text{ if } ij \in \mathscr{A} \setminus \mathscr{D}, \end{aligned} \tag{50}$$

where the nodes (n^{imp}) satisfy

$$\ell^{(n^{\mathrm{imp}})} = \ell^{\mathrm{imp}}, \tag{51}$$

with $\ell^{\mathrm{imp}} \in \{1, 2, \ldots, \ell^{(r)}\}$ itself now regarded as a fitting parameter. This condition states that during probing, the macroscopic conditions must be imposed upon all the nodes of level ℓ^{imp}, instead of the root node, (r). As before, the Sachs iso-stress continuity conditions, Eq. (48), must be imposed upon all the nodes below the level ℓ^{imp}: i.e., $\{(n) : \ell^{(n)} < \ell^{\mathrm{imp}}\}$. This amounts to regarding the original polycrystal as $2^{\ell^{\mathrm{imp}}-1}$ iso-stress sub-polycrystals. The yield stress of each of these sub-polycrystals must be determined. At the onset of yielding, the weakest slip system in each of these sub-polycrystals will activate. By this device, it is ensured that plastic slip occurs in a fixed fraction, $2^{-(\ell^{\mathrm{imp}}-1)}$, of model grains at the onset of yielding, just as in the experiment. As before the macroscopic yield stress is $\sigma_{ij}^{(r)}$, and can be calculated as before using Eq. (5), or (6).

For illustration, consider the 8-grain model polycrystal of Fig. 1. If $\ell^{\mathrm{imp}} = 4$, Eq. (50) is imposed on the root node of this tree. The Sachs analysis will calculate the macroscopic stress at which plasticity incepts in 1 of the 8 grains (fraction: 2^{-3}) in the model polycrystal.

Suppose $\ell^{\mathrm{imp}} = 3$, instead. The conditions, Eq. (50) must now be imposed on the nodes labeled A, and B in Fig. 1. Performing the Sachs analysis on the sub-tree rooted at node A will determine $\sigma_{ij}^{(A)}$ at node A corresponding to plastic inception in 1 out of the 4 grains of the sub-tree below node A. Similarly, Sachs analysis on the sub-tree rooted at node B will determine $\sigma_{ij}^{(B)}$ at node B corresponding to plastic inception in 1 out of the 4 grains of the sub-tree below node B. The macroscopic stress at the root node, $\sigma_{ij}^{(r)}$, can be calculated from the known $\sigma_{ij}^{(A)}$, and $\sigma_{ij}^{(B)}$, using Eq. (5), or (6). This $\sigma_{ij}^{(r)}$ will correspond to the inception of plasticity in 2 out of 8 grains (fraction: 2^{-2}) in the model polycrystal. Similarly, the yield stress corresponding to slip inception in 4 out of 8 grains (fraction: 2^{-1}) can be determined by imposing Eq. (50) on the nodes C, D, E, and F corresponding to $\ell^{\mathrm{imp}} = 2$ in Fig. 1.

Examples of $\bar{D}_{ij}$, and $\bar{\sigma}_{ij}$ appearing in Eq. (50), and relevant to yield surface probing, are now given. To probe the reverse yield point, B, after uniaxial tension in Fig. 2c,

$$\bar{D}_{11} = -1, \text{ and } \bar{\sigma}_{22} = \bar{\sigma}_{33} = \bar{\sigma}_{12} = \bar{\sigma}_{23} = \bar{\sigma}_{13} = 0. \tag{52}$$

Similarly, the yield points D^k and E^k in Fig. 2c can be probed by imposing

$$\begin{aligned} &\bar{D}_{12} = \pm 1, \ \bar{\sigma}_{11} = \sigma_{11}^{\mathrm{ten},k}, \text{ and} \\ &\bar{\sigma}_{22} = \bar{\sigma}_{33} = \bar{\sigma}_{23} = \bar{\sigma}_{13} = 0, \end{aligned} \tag{53}$$

respectively. Let σ_{11}^{A}, and σ_{11}^{B} denote the forward and reverse yield points in uniaxial tension. $\sigma_{11}^{\mathrm{ten},k}$ appearing in Eq. (53) are taken to be the Chebyshev points [54] in the intervening interval:

$$\bar{\sigma}_{11}^{\mathrm{ten},k} = \frac{\sigma_{11}^{A} + \sigma_{11}^{B}}{2} + \frac{\sigma_{11}^{A} - \sigma_{11}^{B}}{2} \cos\left(\frac{(n-k)\pi}{n-1}\right), \tag{54}$$

for $k \in \{1, 2, \ldots, n\}$, where n is chosen sufficiently large to unambiguously draw the yield surface. Presently, $n = 25$. The Chebyshev points are clustered near the edges of the interval to better capture the curvature of the yield surface therein. The reverse and forward yield points are themselves included amongst the $\bar{\sigma}_{11}^{\mathrm{ten},k}$. Likewise, the yield points D^k and E^k in Fig. 2d can be probed by imposing

$$\begin{aligned}&\bar{D}_{11} = \mp 1,\ \bar{\sigma}_{12} = \bar{\sigma}_{12}^{\mathrm{tor},k},\ \text{and}\\&\bar{\sigma}_{22} = \bar{\sigma}_{33} = \bar{\sigma}_{23} = \bar{\sigma}_{13} = 0,\end{aligned} \tag{55}$$

respectively. Again, let σ_{12}^{A}, and σ_{12}^{B} denote the forward and reverse yield points in free-end torsion. $\bar{\sigma}_{12}^{\mathrm{tor},k}$ appearing in Eq. (55) are

$$\bar{\sigma}_{12}^{\mathrm{tor},k} = \frac{\sigma_{12}^{A} + \sigma_{12}^{B}}{2} + \frac{\sigma_{12}^{A} - \sigma_{12}^{B}}{2} \cos\left(\frac{(n-k)\pi}{n-1}\right), \tag{56}$$

for k, and n as in Eq. (54).

The present problem of finding the slip rates, $\dot{\gamma}^{(s),g}$ in all the grains, and the stresses, $\sigma_{ij}^{(n)}$ in all the nodes of the binary tree that satisfy Eqs. (6), (14), (48), and (50), is similar to the problem solved in Eq. (18). The key difference between them is that the macroscopically imposed stress condition is not homogeneous: In Eq. (50), $\bar{\sigma}_{ij}$ is not necessarily zero, unlike in Eq. (10).

The minimisation in Eq. (18) can be readily extended to accommodate the inhomogeneous boundary condition in Eq. (50). To this end, let

$$\hat{\tau}^{(s),g} := \tau^{(s),g} - \sum_{ij \in \mathscr{A} \setminus \mathscr{D}} \bar{\sigma}_{ij} m_{ij}^{(s),g}. \tag{57}$$

Physically, this is equivalent to regarding $\bar{\sigma}_{ij}$, $ij \in \mathscr{A} \setminus \mathscr{D}$, as components of the uniform residual stress in all the grains. Consider the minimisation

$$\min_{\dot{\gamma}^{(s),g}} \sum_{(n_g) \in \mathscr{N}(n^{\mathrm{imp}})} V^{(n_g)} \hat{\tau}^{(s),g} \dot{\gamma}^{(s),g}, \tag{58}$$

subject to the constraints

$$\sum_{(n_g) \in \mathscr{N}(n^{\mathrm{imp}})} \frac{V^{(n_g)}}{V^{(n^{\mathrm{imp}})}} \sum_{s=1}^{S} m_{ij}^{(s),g} \dot{\gamma}^{(s),g} = \bar{D}_{ij}, \tag{59}$$

if $ij \in \mathscr{D}$. In Eqs. (58), and (59), (n^{imp}) is given by Eq. (51). Let $\hat{\sigma}_{ij}^{(n)}$ be the stress components obtained from the dual variables, which represent the Lagrange multipliers that enforce the constraints. Then, the stress components in node (n) are given by

$$\sigma_{ij}^{(n)} = \begin{cases} \hat{\sigma}_{ij}^{(n)}, & \text{if } ij \notin \mathscr{A} \setminus \mathscr{D},\ \text{and} \\ \hat{\sigma}_{ij}^{(n)} + \bar{\sigma}_{ij}, & \text{if } ij \in \mathscr{A} \setminus \mathscr{D}. \end{cases} \tag{60}$$

3.2 Anelastic probing

The present formulation for the onset of anelastic deformation of the model polycrystal is based on that given for a continuum material point by Li and Wagoner [50] and van Liempt and Sietsma [55]. Only the onset of anelastic strain is of interest for probing; the development of finite anelastic strain is not. The polycrystal is probed for anelastic strain in stress space. As with plastic probing, a state of iso-stress obeying Eq. (48) is assumed in the polycrystal during anelastic probing. The onset of anelastic strain is probed along a line in stress space, beginning at $\bar{\sigma}_{ij}^{0}$, and running in the direction $\Delta\bar{\sigma}_{ij}$. Along this line, the applied probing stress $\sigma_{ij}^{(n)}$ in all the nodes (n) of the binary tree model is given by

$$\bar{\sigma}_{ij}(u) = \bar{\sigma}_{ij}^{0} + u\Delta\bar{\sigma}_{ij},\ \text{for } u \geq 0. \tag{61}$$

For example, anelastic probing for the reverse yield point, B, starting from the forward yield point A in Fig. 2c would correspond to $\bar{\sigma}_{11}^{0} = \sigma_{11}^{A}$, $\bar{\sigma}_{22}^{0} = \bar{\sigma}_{33}^{0} = \bar{\sigma}_{23}^{0} = \bar{\sigma}_{13}^{0} = \bar{\sigma}_{12}^{0} = 0$, and $\Delta\bar{\sigma}_{11}^{0} = -1$, $\Delta\bar{\sigma}_{22}^{0} = \Delta\bar{\sigma}_{33}^{0} = \Delta\bar{\sigma}_{23}^{0} = \Delta\bar{\sigma}_{13}^{0} = \Delta\bar{\sigma}_{12}^{0} = 0$. Similarly, for probing the point D^{k} starting from the point C^{k} located on the tensile axis, in Fig. 2c, $\bar{\sigma}_{11}^{0} = \sigma_{11}^{\mathrm{ten},k}$, $\bar{\sigma}_{22}^{0} = \bar{\sigma}_{33}^{0} = \bar{\sigma}_{23}^{0} = \bar{\sigma}_{13}^{0} = \bar{\sigma}_{12}^{0} = 0$, and $\Delta\bar{\sigma}_{12}^{0} = 1$, $\Delta\bar{\sigma}_{11}^{0} = \Delta\bar{\sigma}_{22}^{0} = \Delta\bar{\sigma}_{33}^{0} = \Delta\bar{\sigma}_{23}^{0} = \Delta\bar{\sigma}_{13}^{0} = 0$, where $\sigma_{11}^{\mathrm{ten},k}$ is given by Eq. (54).

As reasoned in connection with Fig. 4, unbowing of the dislocation segments in the loaded slip systems within the near-DDW regions is the principal contribution to anelasticity during probing. This is equivalent to dislocation bowing in the reverse slip system (s') that satisfy Eq. (37). Anelastic strain is proportional to the dislocation density [55]. Therefore, only slip systems with a sizable dislocation density can contribute significant anelastic strain. Dislocation bowing is therefore checked only in those slip systems (s') that satisfy

$$\rho^{(s),g} + \rho^{(s'),g} \geq \varepsilon \left[\max_{(t) \in \{1,2,\ldots,S\}} \rho^{(t),g} + \rho^{(t'),g} \right], \tag{62}$$

where ε is a cut-off parameter. It is found that the results of the anelastic calculations are insensitive to ε; presently, $\varepsilon = 0.1$ is assumed. Dislocations can bow in slip system (s') only if the effective RSS therein increases with increasing u, i.e., if

$$\Delta\bar{\sigma}_{ij} m_{ij}^{(s'),g} > 0. \tag{63}$$

Let $\mathscr{S}^g$ denote the set of slip systems in grain g that satisfy Eqs. (37), (62), and (63). Let $(s') \in \mathscr{S}^g$, and let the state of bowing of the dislocation segments therein be given by $\tau_{\text{state}}^{(s'),g}$. The RSS in slip system (s'), due to the applied stress $\bar{\sigma}_{ij}(u)$ given by Eq. (61) is $\bar{\sigma}_{ij}(u) m_{ij}^{(s'),g}$. Additionally, backstress $\tau_b^{(s'),g}$ given by Eq. (36) acts on (s'), so that the effective RSS given by Eq. (43) is $\tau_{\text{eff}}^{(s'),g} = \bar{\sigma}_{ij}(u) m_{ij}^{(s'),g} + \tau_b^{(s'),g}$. Following Eq. (42), bowing occurs if

$$\bar{\sigma}_{ij}(u_*^{(s'),g}) m_{ij}^{(s'),g} + \tau_b^{(s'),g} = \tau_{\text{state}}^{(s'),g} + \tau_c^{(s'),g}. \tag{64}$$

Substituting Eq. (61) into Eq. (64),

$$u_*^{(s'),g} = \max\left(0, \frac{\tau_{\text{state}}^{(s'),g} + \tau_c^{(s'),g} - \tau_b^{(s'),g} - \bar{\sigma}_{ij}^0 m_{ij}^{(s'),g}}{\Delta\bar{\sigma}_{ij} m_{ij}^{(s'),g}}\right), \tag{65}$$

where $\max(\cdot)$ is introduced to ensure $u_*^{(s),g} \geq 0$.

Minimising $u_*^{(s'),g}$ over all the allowable bowing slip systems in all the grains yields the u at the inception of anelastic strain in the polycrystal:

$$u_{**} = \min_{g} \min_{(s)\in\mathscr{S}^g} u_*^{(s'),g}. \tag{66}$$

The stress at the inception of anelastic deformation is then

$$\sigma_{ij}^{\text{anel}} = \bar{\sigma}_{ij}^0 + u_{**}\Delta\bar{\sigma}_{ij}. \tag{67}$$

The considerations leading up to Eq. (50) in the case of plastic probing are also applied to anelastic probing. Thus, $\sigma_{ij}^{\text{anel}}$ is computed individually for each sub-polycrystal rooted at nodes of level ℓ^{imp} as in Sec. 3.1. Also as before in Sec. 3.1, these stresses are volume averaged to obtain the $\sigma_{ij}^{\text{anel}}$ for the entire polycrystal.

The plastic and anelastic phenomena responsible for the small-offset yield surface in the present model occur within the interior of the grain volume. Contributions from the grain boundary regions through the development of strain-gradients, slip transmission, or grain boundary sliding have not been modeled [56]. This is a limitation of the present model.

4 Parameter fitting

Parameter fitting proceeds in two steps: First, the backstress parameters $\{b_{\text{SH}}, b_{\text{Copl}}, \ldots, b_{\text{LC}}\}$ are fit to the measured experimental yield surface after uniaxial tension, excluding the reverse yield point. Second, the parameters governing the evolution of the friction stress τ_{F0} and $\{c_{\text{SH}}, c_{\text{Copl}}, \ldots, c_{\text{LC}}\}$ are fit to match the reverse yield point. This two-step approach is taken because it is found impossible to fit the reverse yield point without invoking anelasticity.

The first step of fitting is performed using the Nelder and Mead [57] algorithm. The algorithm starts with an initial guess of the backstress parameters, with each b_{i} in Eq. (32) being drawn from a uniform distribution over the interval $[-1, 1]$. Within each iteration, the dislocation evolution parameters, K, and f of the storage-annihilation Eq. (25), and τ_{a0} of Eq. (27) are fitted to the post-relaxatic stress-strain curve, also using the Nelder-Mead algorithm. The cost function is the r.m.s. error between the experimentally measured post-relaxatic forward yield stress, and the predicted one after the tensile loading. With the K, and f fitted, the yield surface is plastically probed, and the r.m.s. error between the measured and predicted yield surfaces is calculated. The reverse yield point is not included in the r.m.s. error computation. By translating, rotating, and distorting a six-vertex simplex in the six-dimensional space of $\{b_{\text{SH}}, b_{\text{Copl}}, \ldots, b_{\text{LC}}\}$, the Nelder-Mead iterations attempt to decrease the cost function. The six-dimensional space of $\{b_{\text{SH}}, b_{\text{Copl}}, \ldots, b_{\text{LC}}\}$ has multiple local minima, each with its basin of attraction [58]. When a vertex of the Nelder-Mead simplex enters a basin of attraction, the remaining vertices follow suit, causing the simplex volume to decrease with each additional iteration. The algorithm terminates when the volume of the simplex becomes smaller than a pre-set threshold. The foregoing process is repeated for a number of ℓ^{imp}.

In order to minimise the cost function, it is desirable to sample a number of local minima.

To that end, several (thirty two, presently) independent instances of the Nelder-Mead program each starting with randomly drawn initial guesses, $b_{\mathrm{i}} \in [-1, 1]$, are run in parallel. The set of parameters that yield the smallest r.m.s. error amongst all the instances is taken to be the best-fitting set of parameters.

Fitting is performed on the yield surfaces measured after tensile deformation only. With the same parameters, yield surfaces after torsion are predicted, and compared with the experimental yield surfaces of Khan et al. [29]. This provides a test of the generality of the model, and of the material parameters.

Fitting the friction stress parameters τ_{c0}, and $\{c_{\mathrm{SH}}, c_{\mathrm{Copl}}, \ldots, c_{\mathrm{LC}}\}$ that appear in Eq. (40) is considerably more straightforward. The interaction parameters are required to take the form

$$\{c_{\mathrm{SH}}, c_{\mathrm{Copl}}, \ldots, c_{\mathrm{LC}}\} = \psi_c\{\iota_1, \iota_2, \ldots, \iota_6\}, \tag{68}$$

where each $\iota_{\mathrm{i}} \in \{0, 1, \ldots, I\}$, and ψ_c is a positive real parameter to be determined. Presently, $I = 3$. According to Eq. (68), $(I+1)^6$ forms of the friction stress interaction parameters must be probed. For each of these forms, $\tau_{c0} \geq 0$, and $\psi_c \geq 0$ are determined using Nelder-Mead minimization of the cost function. The cost function is the r.m.s. error between the predicted and experimental reverse yield point at the all the strain levels studied experimentally. Once ψ_c is obtained, the best fit $\{c_{\mathrm{SH}}, c_{\mathrm{Copl}}, \ldots, c_{\mathrm{LC}}\}$ can be inferred using Eq. (68).

It is noted that interaction coefficients governing the backstress and the friction stress are not amenable to fitting by hand. This is because the rate-independence of the present model makes the variation of the cost function non-smooth over the parameter space. For this same reason, the automated fitting procedure outline above uses the derivative-free Nelder-Mead algorithm extensively.

5 Results and discussion

Khan et al. [29] experimentally probed the yield surface of an Al 1100 tubular specimen after subjecting it to prestrain $\epsilon_{11}^{\mathrm{pre}} = 2\%$, $\epsilon_{11}^{\mathrm{pre}} = 8\%$, and $\epsilon_{11}^{\mathrm{pre}} = 16\%$ strain in uniaxial tension. They also obtained the yield surface after imposing $\gamma_{12}^{\mathrm{pre}} = 4\%$, $\gamma_{12}^{\mathrm{pre}} = 10\%$, and $\gamma_{12}^{\mathrm{pre}} = 20\%$ engineering shear strain through free-end torsion. It is aimed presently to replicate their yield surface measurements computationally.

Khan et al. [29] stress-relaxed the specimen at constant strain after loading, and before probing for the yield surface. It was noted in Sec. 2.3.3 that $|\tau_{\mathrm{state}}^{(s),g}|$ diminishes during strain-holding. Since it is presently not possible to estimate the magnitude of its reduction [59], it is assumed that

$$\tau_{\mathrm{state}}^{(s),g} = 0. \tag{69}$$

In words, it is assumed that the dislocation segments between pinning points become straight after strain-holding.

5.1 Loading

The balanced binary tree model of Sec. 2.1 representing a polycrystalline aggregate comprised of $2^{10} = 1024$ grains, each of volume fraction 2^{-10}, is used to simulate loading in uniaxial tension, and free-end torsion. The balanced binary tree has $\ell^{(r)} = 11$ levels. As the initial texture of the Khan et al. [29] specimen is not available, the simulations start with grains assigned lattice orientations drawn from the uniformly random texture. This assumption is supported by the observation that the initial yield surface of the experimental material is well-fitted by the isotropic von Mises criterion [29]. Also, assuming the tubular specimen were extruded, the grain boundaries can be expected to align preferentially with the radial direction. To reflect this, the initial planar interfaces between sibling nodes in the binary tree are randomly assigned normals oriented within a right circular cone of apex angle 30°, whose axis is aligned with the radial direction.

The parametric fitting procedure of Sec. 4 was run to fit the three subsequent yield surfaces measured by Khan et al. [29] after tensile prestrains of 2%, 8%, and 16%. Standard values assumed for the well-known material parameters of aluminium are shear modulus, $\mu = 26.32$GPa, and the magnitude of the Burgers vector, $b = 2.8622$Å. The grain size in Eq. (25) was taken to be $D = 36$ μm. In Eq. (34), ρ^{ann} was taken to be 10^6 /m^2. The values of the initial hardness, and interaction parameters corresponding to hardening, backstress, and friction stress, obtained from the fitting algorithm,

		Hardening, Eq. (27)	Backstress, Eq. (36)	Friction stress, Eq. (40)
Initial hardness		$\tau_{a0} = 19.3$ MPa		$\tau_{c0} = 6.10$ MPa
Interaction parameters	SH	$a_{\mathrm{SH}} = 0.122$	$b_{\mathrm{SH}} = 0.7193$	$c_{\mathrm{SH}} = 0$
	Copl	$a_{\mathrm{Copl}} = 0.122$	$b_{\mathrm{Copl}} = 1.3868$	$c_{\mathrm{Copl}} = 2.5418$
	CS	$a_{\mathrm{CS}} = 0.625$	$b_{\mathrm{CS}} = 0.8203$	$c_{\mathrm{CS}} = 0.8473$
	HL	$a_{\mathrm{GJ}} = 0.070$	$b_{\mathrm{GJ}} = 0.4163$	$c_{\mathrm{GJ}} = 0$
	GJ	$a_{\mathrm{HL}} = 0.137$	$b_{\mathrm{HL}} = 1.6267$	$c_{\mathrm{HL}} = 0.8473$
	LC	$a_{\mathrm{LC}} = 0.122$	$b_{\mathrm{LC}} = -0.8511$	$c_{\mathrm{LC}} = 1.6945$

Table 1: Parameters quantifying the physical mechanisms of slip system hardening, backstress, and friction stresses in the present model. The interaction parameters for slip system hardening, a_{i}, are taken from Kubin et al. [43].

are given in Table 1. The optimal values of parameters appearing in Eq. (25) were found to be $K = 26.226$, and $f = 11.276$. The probing level in Eq. (51) is taken to be $\ell^{\mathrm{imp}} = 6$.

Fig. 5 shows the evolution of the total dislocation density, averaged over all the grains,

$$\langle\rho\rangle = \frac{\sum_g \sum_{s=1}^{S} \rho^{(s),g}}{\sum_g 1}, \tag{70}$$

during tensile and torsional loading. In Eq. (70), and henceforth, $\langle\cdot\rangle$ denotes averaging over all the slip systems in all the grains. The average dislocation density evolves remarkably similarly along both loading paths. The scatter in dislocation density evolution is also small relative to the average value.

Fig. 6 shows the average forest hardening, average backstress, and average friction stress for loading along both the tensile and torsional loading paths. The standard deviation of the corresponding quantities amongst grains is also indicated by error bars. In the case of the backstress, $\langle -\tau_b \rangle$, the average is taken only over the unloaded slip systems. Roughly, the average negative backstress is about half of the average forest hardness. The friction stress is, however, considerably greater than the forest hardness, and shows considerably greater scatter from grain to grain. This is because the friction stress in Fig. 6 pertains to the localised region near the DDWs, as anelastic effects are confined to that region only. The friction stress in the cell interiors is expected to be considerably smaller.

As in Fig. 5, the evolution of $\langle\tau_a\rangle$, $\langle\tau_b\rangle$, and $\langle\tau_c\rangle$ with von Mises strain is remarkably similar for both tensile and torsional loading. It is known that textural and substructural effects cause the tensile, compressive, and torsional plastic responses to diverge from each other with increasing von Mises strain [22, 60]. It follows that the present strain levels are small enough for this divergence to be insignificant.

Fig. 7 shows the texture evolution during tensile and torsional loading through $\{111\}$ pole figures. The initial texture is random. Under tensile loading, grains are seen to rotate to align the tensile axis x_1 with $\{111\}$, or $\{100\}$ poles, consistent with the observations in the literature [61]. Under torsional loading also, the developed texture is consistent with observations in the literature [62]. Thus, qualitatively distinct, albeit relatively weak textures develop in the tensile and torsional loading modes over the strain range of present interest. The weakness of the developed texture is consistent with the similar evolution of state seen in Figs. 5, and 6 during both tension and torsional loading.

5.2 Yield surface probing

Fig. 8a shows the points on the yield surface of Al 1100 measured by Khan et al. [29] after 2%,

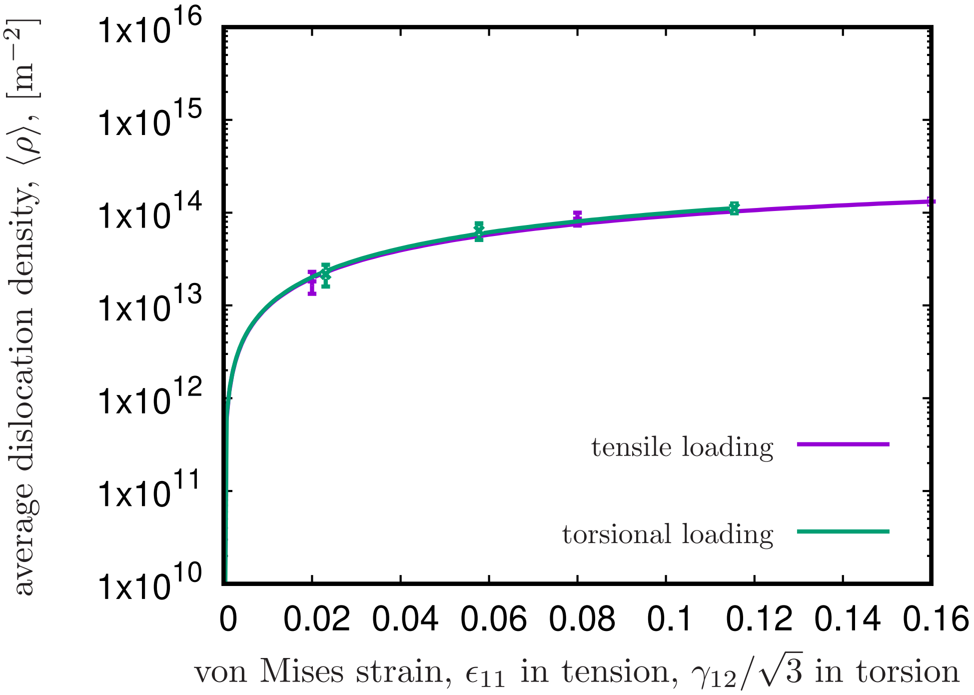

Fig. 5: Evolution of the average dislocation density in grains with strain, during tensile and torsional loading. The errors bars denote the standard deviation amongst grains.

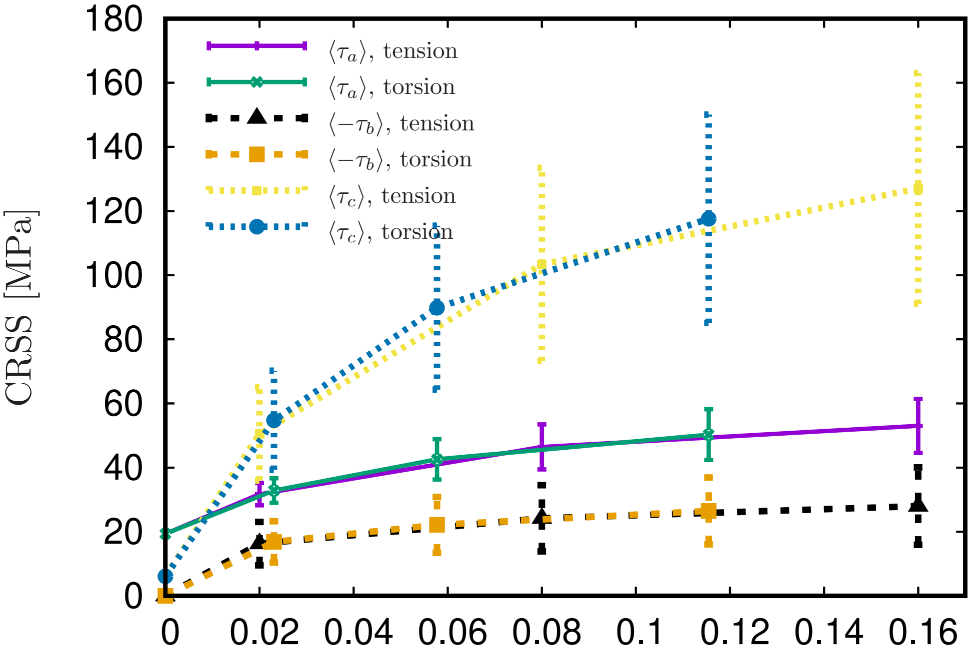

Fig. 6: Evolution of the average forest hardening, $\langle\tau_a\rangle$, negative backstress, $\langle\tau_b\rangle$, and friction stress, $\langle\tau_c\rangle$, in grains with strain, during tensile and torsional loading. The errors bars denote the standard deviation amongst grains.

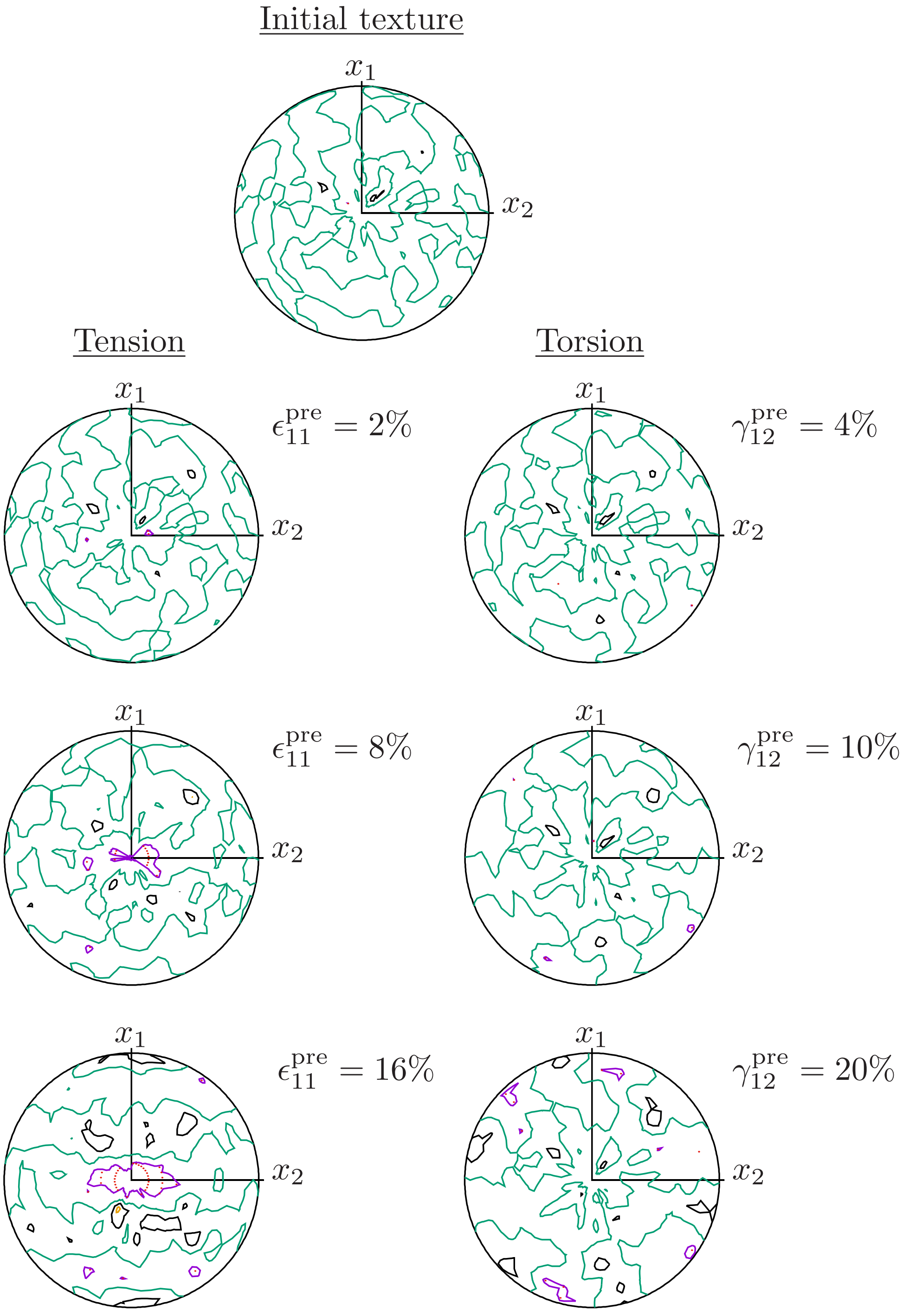

Fig. 7: Predicted {111} pole figures during tensile (left column) and torsional (right column) deformation beginning with a random initial texture. x_1 denotes the axial direction, and x_2 the circumferential direction. The levels are $\{0.5, 1.0, 1.5, 2.0\}\times$ m.r.o: Regions with texture intensity smaller than 0.5 are indicated by dots.

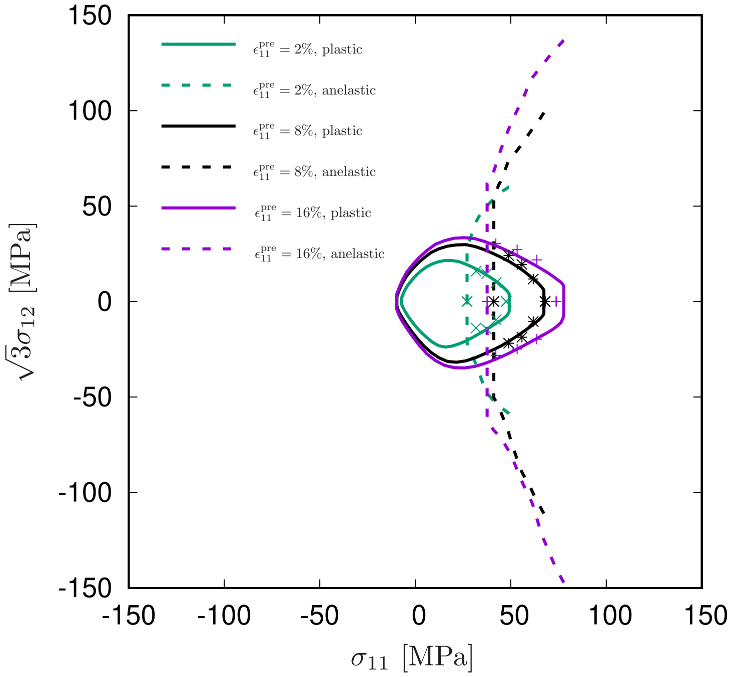

(a) after tensile prestrain, $\epsilon_{11}^{\text{pre}}$

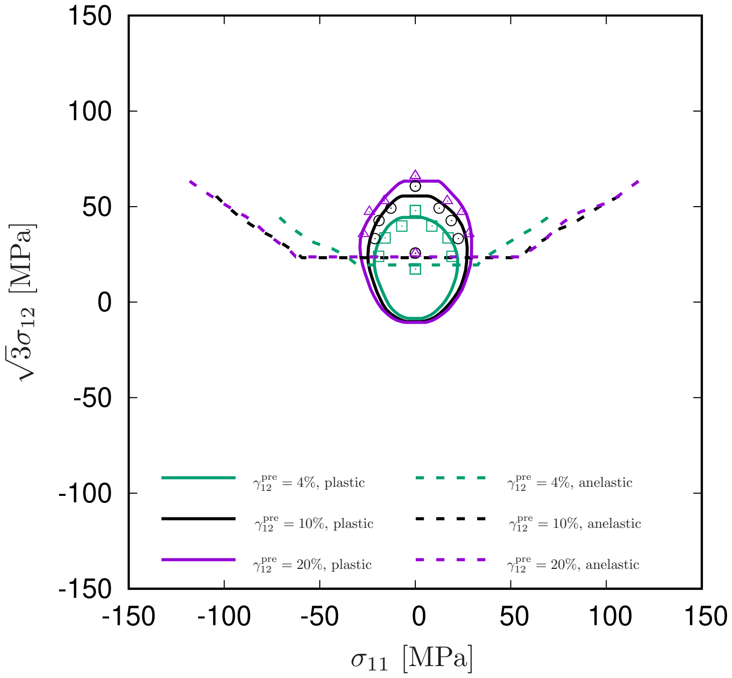

(b) after torsional prestrain, γ_{12}^{pre}

Fig. 8: Subsequent yield surfaces of Al1100 predicted by the present plastic, and anelastic computations after various (a) tensile, and (b) torsional prestrains. The experimental measurements of Khan et al. [29] are indicated by points.

8%, and 16% tensile prestrains. It also shows the yield surfaces predicted through plastic probing, as described in Sec. 3.1. At all the three prestrain levels, the predictions capture both the forward yield stress, and the yield surface curvature satisfactorily. The predicted yield surface has a blunt nose, showing that the model polycrystal requires a non-zero shear stress to yield in shear even when loaded to the tensile yield point.

The reverse yield point as predicted by plastic probing does show a Bauschinger effect: For all the three prestrains, the reverse yield point is greater than the negative of the forward yield point. Even so, the predicted reverse yield point misses the experimentally measured reverse yield point by a large margin. In fact, the predicted reverse yield point has the opposite sign as the measured one. This is a consequence of Eq. (39): Since the effective CRSS of all the slip systems remains positive, yielding in the forward and reverse directions will necessarily require applied stresses of opposite sign. It is therefore not possible to capture the reverse yield point through plastic probing.

Fig. 8a also shows the yield surface obtained from anelastic probing. It is seen that the anelastic yield surface captures the reverse yield point after the three prestrains very well. It even captures the experimental observation that the reverse yield point moves non-monotonically with the prestrain level: increasing from 2% to 8%, and then decreasing. Elsewhere along the tensile axis, i.e., for other $\sigma_{11}^{\text{ten},k}$ given by Eq. (54), anelastic probing results in a much larger yield surface than the plastically probed yield surface.

The non-monotonicity of the predicted reverse yield point is surprising since the friction stress, $\tau_c^{(s),g}$, given by Eq. (40), monotonically increases with dislocation density, which increases with plastic strain. This shows that the slip system interactions, c_{st}, are responsible for the non-monotonicity. On the basis of this observation, it is speculated that slip system interactions underlie the non-monotonic elastic-anelastic transition stress reported in a number of materials by Li and Wagoner [50].

As noted in Sec. 1, previous studies have measured forward and reverse yield points of opposite sign, and even predicted them using polycrystal plasticity models. The key difference between those measurements, and that of Khan et al. [29] is that the magnitude of the strain offset used to define yielding in the former is many orders of magnitude greater than that in the latter. It thus appears that when probing for the reverse yield point, the initial deviation from linearity in the stress-strain response, within the range of small-offset probing, is caused by anelastic deformation. This mechanism then gives way to plasticity, which underlies the large-offset regime.

Keeping all the material parameters listed in Table 1, and elsewhere unchanged, the plastic and anelastic yield surfaces are predicted after three levels of torsional prestrain. These predictions are compared with the experimental measurements of Khan et al. [29] in Fig. 8b. Again, the forward yield point, and the lateral surfaces of the yield surface are satisfactorily captured by the plastic probing simulations. Again, the reverse yield point is not captured by plastic probing, but is reasonably captured by anelastic probing. Although the model parameters are fit to the yield surfaces of the tensile prestrained specimen, the model captures the subsequent yield surfaces of torsionally prestrained specimen also.

The inner envelope formed by the plastically and anelastically probed yield surfaces is compared with the experimental measurements in specimen subjected to both tensile and torsional prestrains in Fig. 9. A satisfactory fit of the measurements is observed. It is concluded that the deviation from linearity during yield surface probing in the experiment can be attributed to two distinct physical mechanisms: At the forward yield point, and along the lateral surfaces, plasticity causes the inelastic deviation from linearity. At the reverse yield point, anelasticity is responsible for the same effect.

It is recalled from Sec. 2.2 that the present model grains are assumed rigid plastic, whereas physical aluminium grains obey anisotropic elasticity before yielding. Using the anisotropic elastic moduli measured at room temperature for Al crystals by Vallin et al. [63], and the analytical formulae derived by Cazzani and Rovat [64], the maximum and minimum Young's moduli for Al are obtained as 75.6 GPa, and 63.3 GPa, along the $\langle 111 \rangle$, and $\langle 100 \rangle$ directions, respectively. The directional variation of Young's modulus of an Al crystal is thus about 69.4 GPa ±9%. Assuming that the grains of the polycrystal subjected to

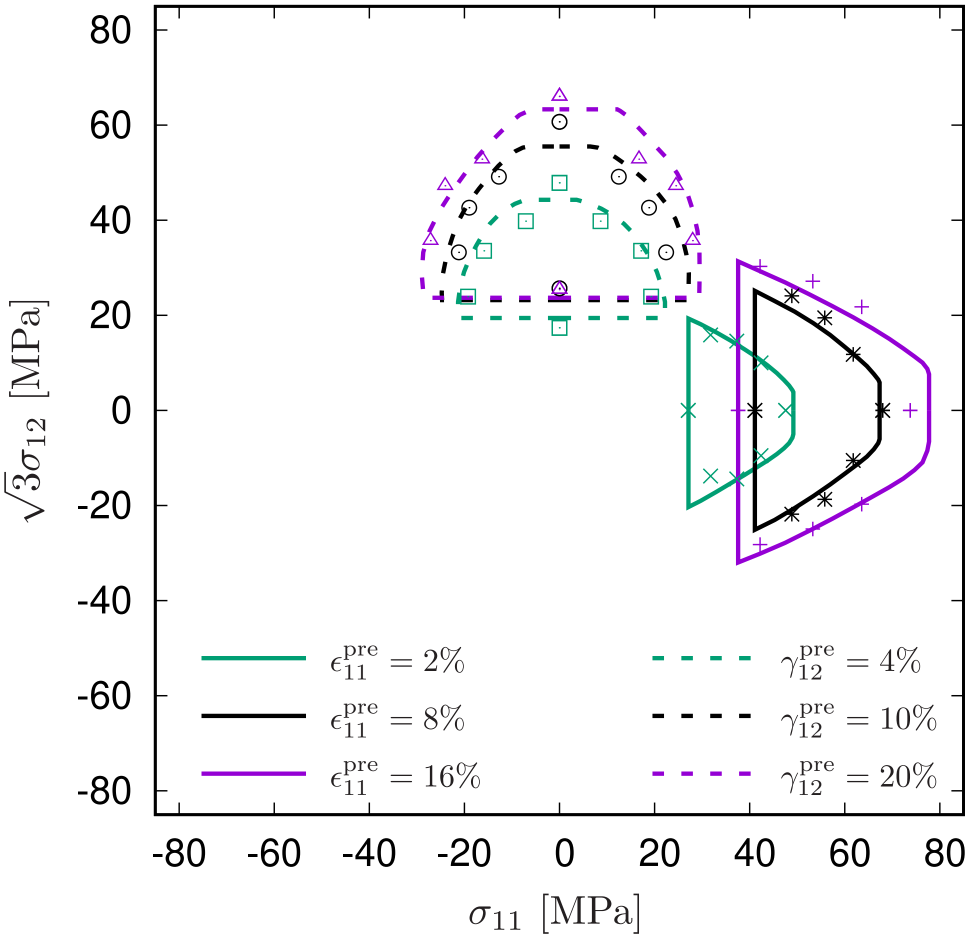

Fig. 9: Inner envelope of the predicted subsequent plastic and anelastic yield surfaces of Fig. 8 after imposing various prestrains in uniaxial tension (solid), and free-end torsion (dashed). The experimental measurements of Khan et al. [29] are also indicated.

uniaxial tension obey the limiting iso-strain condition, the tensile stress variation is thus bounded by 9%. A comparably small scatter is also expected for the shear modulus, and therefore, shear stress fluctuation in the grains. Thus, the error due to neglecting the anisotropic elasticity of Al grains is small.

The algorithmic procedure of Sec. 4 finds multiple local minima. The parameters listed in Table 1 correspond to the best local minimum with the smallest r.m.s. error. Yield surfaces determined using the parameter sets corresponding to the second, third, fourth, and fifth best local minima have been computed, and compared with the measured yield surfaces. These latter predictions resulted in qualitatively poorer fits of the experimental yield surface measurements than that shown in Fig. 9. Thus, within the scope of the parameter fitting procedure, the parameters listed in Table 1 represent unique values.

5.3 Role of backstress, and anelasticity

The role of backstress, and anelasticity are presently assessed. Fig. 10 shows the yield surfaces computed by setting $b_{st} = 0$ in Eq. (38), and $c_{st} = \infty$ in Eq. (40), after prestraining in tension, and torsion. These parameter choices correspond to completely suppressing the backstress and anelastic effects.

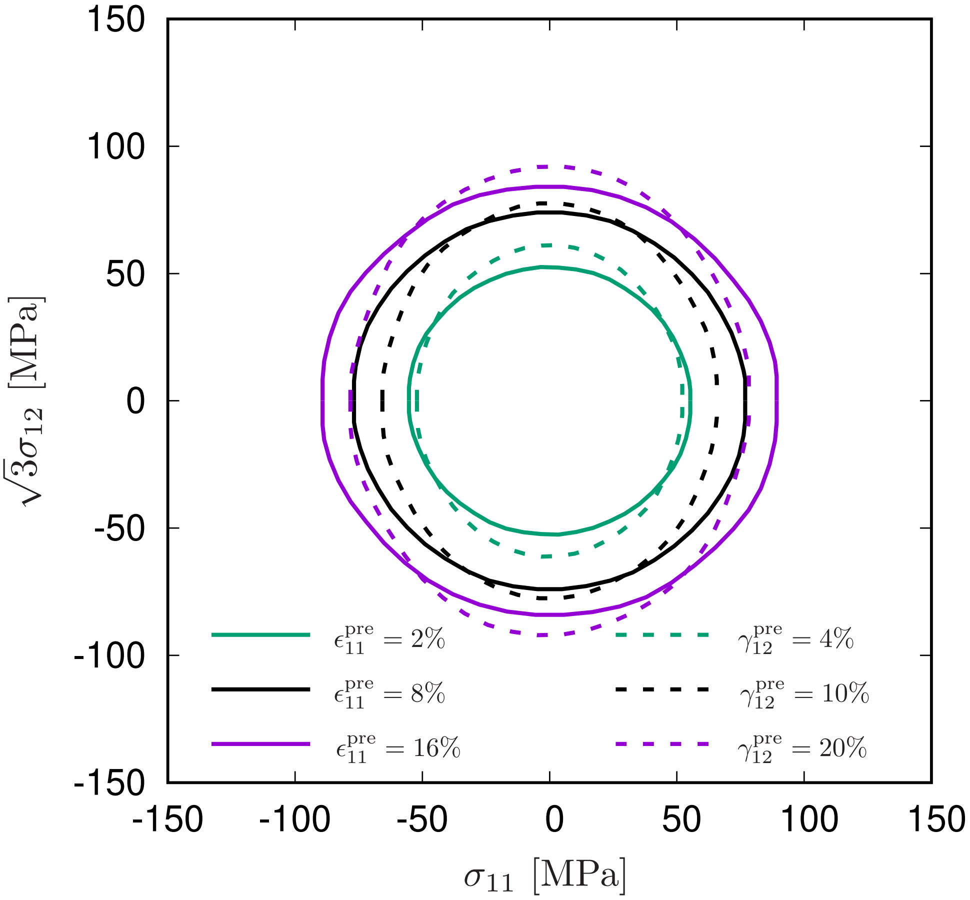

Fig. 10: Comparison of the yield surfaces predicted by the plasticity model without backstress after tensile and torsional prestrains.

The yield surfaces predicted in the absence of backstress and anelasticity are elliptical, with the major axis of the ellipse aligned with the prestraining direction, and the minor axis transverse to it: The yield surfaces obtained after tensile prestrain are elongated along the σ_{11} axis, while those obtained after torsional prestrain are elongated along the $\sqrt{3}\sigma_{12}$ axis. This anisotropy between the loading and transverse directions is a consequence only of the texture, and of the forest hardening. They predict a symmetric response in the prestraining, and opposite directions. This implies that the different curvatures of the yield surface in the prestrain, and opposite directions must be entirely attributed to backstress, and anelasticity effects.

It is next sought to determine the individual contribution of each b_{i} in Eq. (32) to the shape of the yield surface. This is done by considering two extreme scenarios. First, b_{i} is set to its value in Table 1, and all b_{j}, $\text{j} \neq \text{i}$ are set to zero. The yield surfaces so predicted are shown in the left column of Fig. 11. Second, b_{i} is set to zero, while the other parameters b_{j}, $\text{j} \neq \text{i}$ are assigned values from Table 1. The resulting predictions are shown in the right column of Fig. 11. It is expected that if a particular b_{i} were especially important, the predicted yield surfaces in the left column will qualitatively agree with the experimentally measured ones. On the other hand, if b_{i} were unimportant, i.e., if the effect of its omission were small, it is expected that the predicted yield surfaces in the right column will resemble the experimental measurements.

Consider the predicted plastic yield surfaces shown in Fig. 11c, which are obtained by retaining the value of b_{Copl} from Table 1, while setting all other b_{i}, $\text{i} \in \{\text{SH}, \text{CS}, \text{HL}, \text{GJ}, \text{LC}\}$ to zero. It

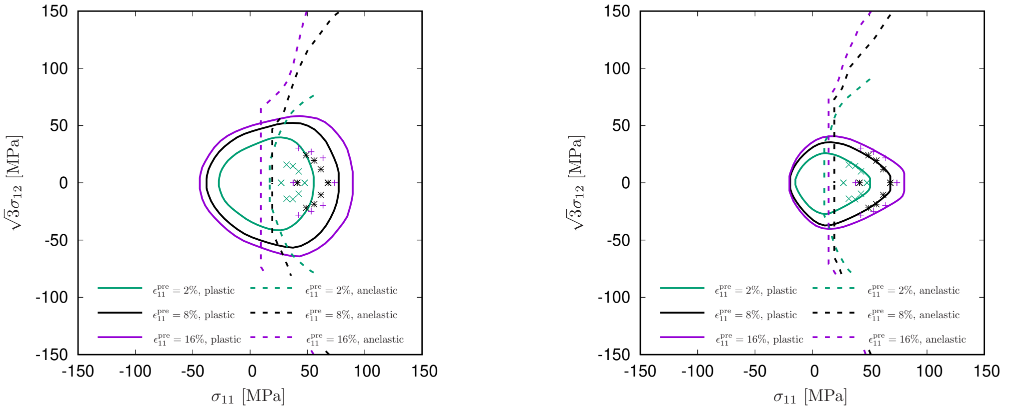

(a) b_{SH} from Table 1, other $b_{\mathrm{i}} = 0$

(b) $b_{\mathrm{SH}} = 0$, other b_{i} from Table 1

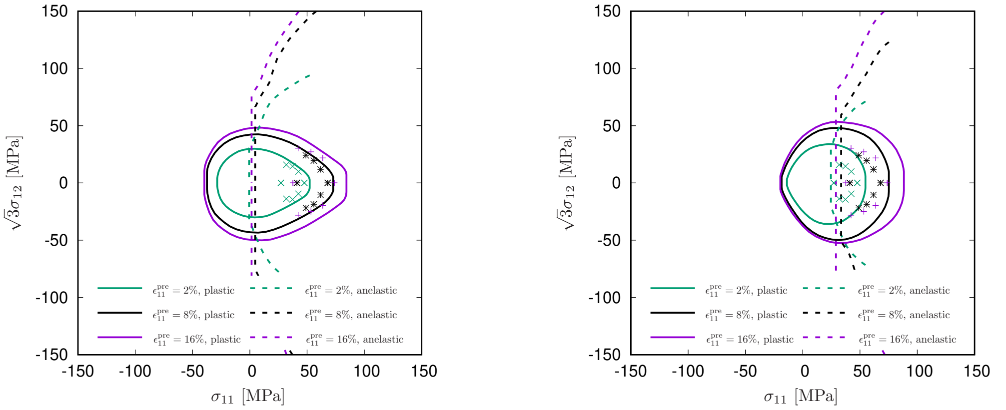

(c) b_{Copl} from Table 1, other $b_{\mathrm{i}} = 0$

(d) $b_{\mathrm{Copl}} = 0$, other b_{i} from Table 1

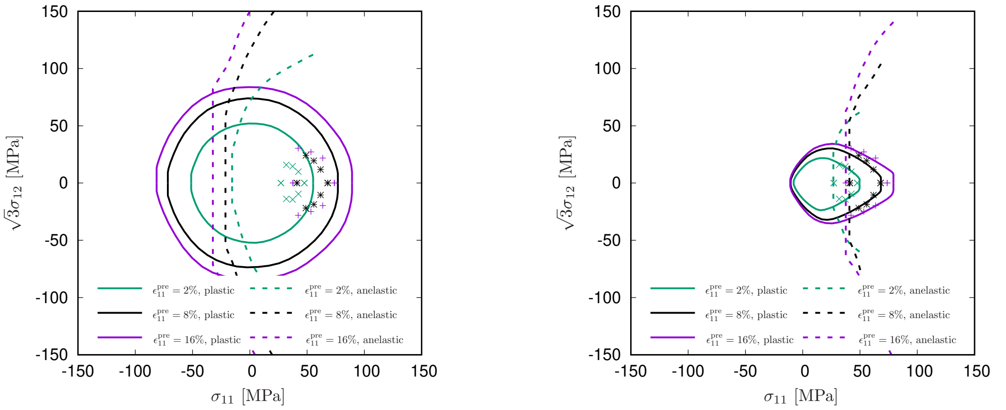

(e) b_{CS} from Table 1, other $b_{\mathrm{i}} = 0$

(f) $b_{\mathrm{CS}} = 0$, other b_{i} from Table 1

is seen that the curvature of the nose is qualitatively captured. The predictions obtained by omitting b_{Copl}, while retaining the other b_{i}, are shown in Fig. 11d. The predicted yield surfaces in Fig. 11d are much blunter at the nose. They compare poorly with the measurements. These observations indicate that b_{Copl} plays a central role in capturing the shape of the plastic yield surface.

Barring the second row in Fig. 11 corresponding to b_{Copl}, it is seen that in all the other rows, a poor comparison between the predictions and

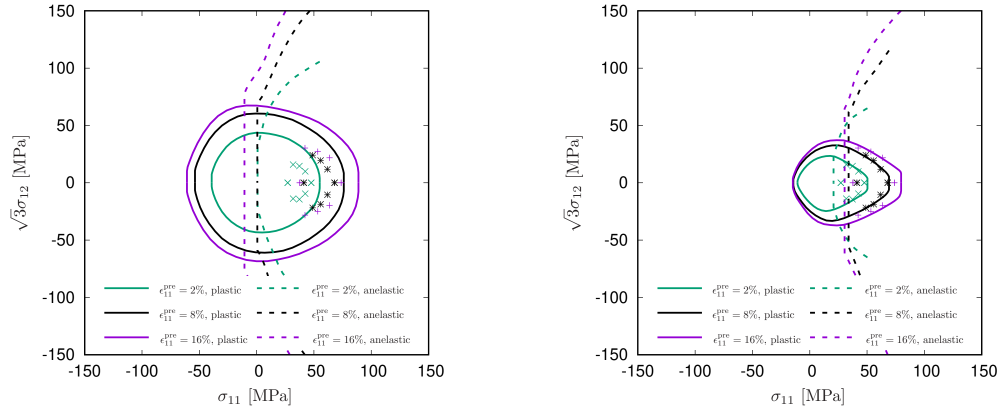

(g) b_{HL} from Table 1, other $b_{\mathrm{i}} = 0$

(h) $b_{\mathrm{HL}} = 0$, other b_{i} from Table 1

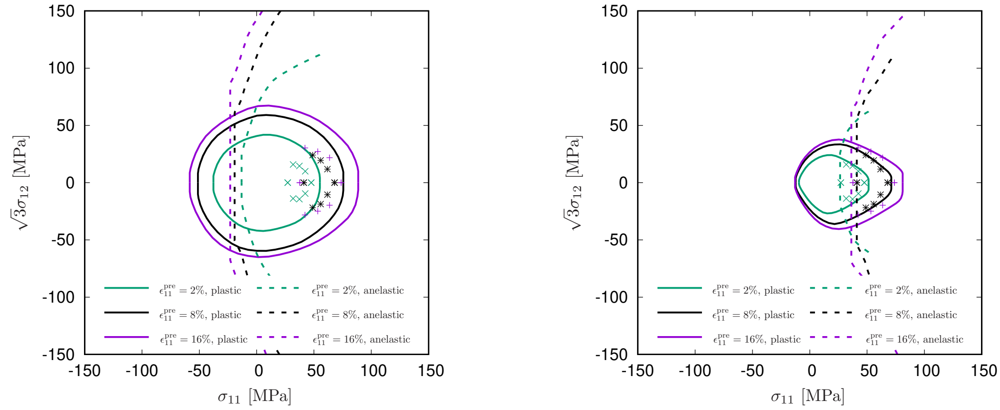

(i) b_{GJ} from Table 1, other $b_{\mathrm{i}} = 0$

(j) $b_{\mathrm{GJ}} = 0$, other b_{i} from Table 1

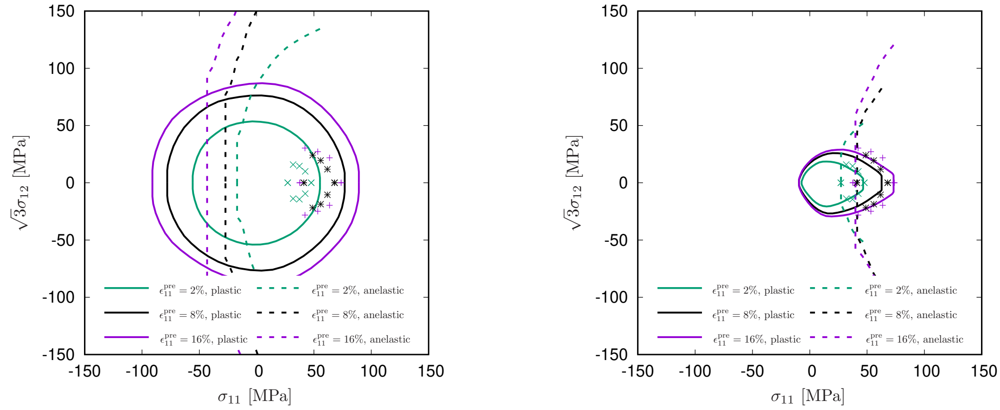

(k) b_{LC} from Table 1, other $b_{\mathrm{i}} = 0$

(l) $b_{\mathrm{LC}} = 0$, other b_{i} from Table 1

Fig. 11: To gauge the individual effect of each b_{i} on the predicted yield surfaces, two types of parametric variations are considered. In the figures of the left column, one interaction, b_{i}, is retained, while setting all the others to zero. In the right column, $b_{\mathrm{i}} = 0$, while retaining all the other interactions.

measurements is obtained in the left column, and a qualitatively reasonable comparison is obtained in the right column. This also indicates that b_{i}, i $\in \{\mathrm{SH}, \mathrm{CS}, \mathrm{HL}, \mathrm{GJ}, \mathrm{LC}\}$ contribute less than b_{Copl} to the shape of the predicted plastic yield surfaces. Of these contributions, the one shown in Fig. 11f is noteworthy. It shows that setting $b_{\mathrm{CS}} = 0$, while retaining the values of the other b_{i} leads to practically the same predictions as in Fig. 8a. This points to the negligible contribution of b_{CS} to the plastic yield surfaces. In summary, the predicted plastic yield surfaces are determined principally by b_{Copl}, followed by b_{SH}, b_{HL}, b_{GJ}, and b_{LC}. They are almost insensitive to b_{CS}.

The backstress, controlled by b_{i}, also partly governs the anelastic response, and hence the predicted reverse yield point. The left column of Fig. 11 shows the predicted anelastic yield surfaces obtained by imposing each b_{i} individually. None of these predictions agree with the measured reverse yield points. Thus, the anelastic response, unlike the plastic response, is not dictated by any of the b_{i} individually. In the right column, it is seen that omitting b_{SH}, b_{Copl}, and b_{HL} results in a larger gap between the predicted and measured reverse yield points, as seen in Figs. 11b, 11d, and 11h, respectively, than that obtained by omitting b_{GJ}, and b_{LC}, as seen in Figs. 11j, and 11l, respectively. Fig. 11f shows that omitting b_{CS} hardly disturbs the quantitative agreement between the predicted and experimental reverse yield points. Thus, the anelastic reverse yield point predictions are determined by b_{SH}, b_{Copl}, and b_{HL} principally, followed by b_{GJ}, and b_{LC}. They are nearly insensitive to b_{CS}.

Although not shown, the above observations apply also to specimen subjected to torsional prestrain. Further, a similar exercise to determine the important interaction parameters c_{i} that significantly affect the predicted reverse yield point reveals that all the c_{i}, except c_{CS}, are comparably important.

The insensitivity of the predicted plastic and anelastic yield surfaces to b_{CS}, and c_{CS} derives from the much larger value of a_{CS} compared to the other a_{i}, as seen in Table 1. Let (s) and (t) be slip systems such that $a_{st} = a_{\mathrm{CS}}$, and let (t') be the reverse slip system of (t). Let slip system (s) activate during the loading stage. Then, according to Eq. (27), slip systems (t), and (t') will experience rapid forest hardening. This will suppress slip activity, dislocation density build up (Eq. (25)), and hence, anelastic strains (Eq. (62)) in the slip systems (t), and (t'). The large forest hardness of the slip systems (t), and (t') will also result in a large CRSS (Eq. (38)), which will suppress their activation during plastic probing. They will thus not participate in determining either the anelastic response or the plastic response during probing, making the predicted yield surfaces independent of b_{CS}, and c_{CS}.

Finally, it is noted from Table 1 that coplanar and Lomer-Cottrell interactions are the largest contributors to the hardening of the friction stress. This suggests that slip activity in the coplanar and Lomer-Cottrell slip systems of a given slip system (s) produce the most dislocation debris that serve to oppose dislocation bowing and unbowing. Notably, the self hardening interaction coefficient, c_{SH}, is zero, indicating negligible friction stress hardening in a slip system due to its own slip activity.

5.4 Comparison with previous works

Experimental analyses of the dislocation content of DDW in fcc copper [48] and fcc aluminium [49] have found sets of dislocations from coplanar slip systems, and Lomer-Cottrell (LC) locks. According to the present results, however, the LC contribution to the backstress appears to be smaller than that of Copl. A plausible cause for this observation is that the edge part of the Lomer-Cottrell junction does not react elastically with the screw part of incoming dislocations. This reduces the stand-off distance, i.e., reduces the range of the backstress [47]. The reduced range may be reflected in $b_{\mathrm{LC}} < b_{\mathrm{Copl}}$.

The case $b_{\mathrm{SH}} \neq 0$ and $b_{\mathrm{i}} = 0$, for $i \neq \mathrm{SH}$, shown in Fig. 11a is of interest also because it corresponds approximately to the substructural model of Wen et al. [24] after monotonic loading. To see this, it is recalled that the backstress in the Wen et al. [24] model is given by Eq. (30). At the end of monotonic loading, assuming $b_{\mathrm{SH}} \neq 0$ and $b_{\mathrm{i}} = 0$, for $i \neq \mathrm{SH}$, Eq. (36) becomes

$$\tau_b^{(s'),g} = -\tau_a^{(s),g} \left(1 - \exp(-b_{\mathrm{SH}})\right), \qquad (71)$$

where (s), and (s') have the same meanings as in Eq. (30). By identifying f_B^s with $(1 - \exp(-b_{\mathrm{SH}}))$, it is clear that when slip system interactions are taken away, the present backstress formulation reduces to that of Wen et al. [24]. Further, substituting $b_{\mathrm{SH}} = 0.7193$ from Table 1 results in $1 - \exp(-b_{\mathrm{SH}}) \approx 0.51$, which is almost equal to the parametric value $f_B^s = 0.5$ fit by Wen et al. [24]. It is thus seen that in the limiting case of backstress governed by self-hardening only, the present model replicates the Wen et al. [24] model in the special case of monotonic loading. However, as Fig. 11a shows, the predicted yield surface in this limit does not compare even qualitatively with the experimental one.

The present predictions of the yield surface of annealed 1100 Al are now compared with those of two modeling works in the literature. As noted in Sec. 1, Liu et al. [19] model the polycrystal as a single grain with 30 slip components, whose interactions determine their hardening. In their work, self and latent hardening contributions are governed by the projection of the Schmid tensors of the slip components, $m_{ij}^{(s)} m_{ij}^{(t)}$, in the present notation. This factor also appears in the present Eq. (33). By suitable choice of the hardening parameters for annealed 1100 Al, Liu et al. [19] reasonably captured the advancing forward yield point with increasing strain, and the increasing cross-effect with increasing strain in tension. However, their predicted forward and reverse yield points in torsion underestimate, and overestimate the experimental values, respectively. Also, while their predictions capture the sharp curvature near the forward yield point, their model predicts a less blunt yield surface than the measurements near the reverse yield point, both in tension and in torsion. Their predictions also do not capture the order of reverse yielding with prestrain.

The phenomenological model of Pietryga et al. [18], discussed in Sec. 1, also captures all the aspects of the yield surfaces after tensile prestrain. However, their torsional yield surfaces overestimate the reverse yield point by large margins. A common feature of the aforementioned works is that they explain reverse yielding through plasticity. On the contrary, in the present work, anelasticity determines the reverse yield point. If the present model were to capture the large Bauschinger effect though plasticity alone, a large backstress would be required, resulting in the violation of Eq. (39). This would jeopardise the stability of the resulting material model.

The models of Liu et al. [19] and Pietryga et al. [18] do suffer from stability issues. Liu et al. [19] do not enforce any conditions for plastic stability, and the present Eq. (39) may be violated in at least some of the their slip components. Nevertheless, Liu et al. [19] do not detect instability because, in their computations, only the elastic and damage components bear the applied stress. Plastic deformation is calculated in an uncoupled way: While the plastic deformation is determined by stress, plastic deformation does not influence stress. Pietryga et al. [18] noted that their predicted subsequent yield surfaces are not necessarily convex, which may impact the stability of numerical simulations. In summary, the present formulation invoking two mechanisms, plasticity, and anelasticity, captures the measured yield surface while also guaranteeing the stability of inelastic deformation. This guarantee is absent in the aforementioned works.

6 Conclusions

A novel physical model of substructural evolution has been proposed. The model accounts for two modes of inelastic deformation, viz., rate-independent plasticity, and anelasticity. It accounts for hardening, backstress, and friction stress evolution in the substructure, all while accounting for slip system interactions. An algorithm for fitting the model parameters is also proposed.

The model has been used to computationally simulate the loading and probing of the small-offset yield surface. Model parameters are fitted to the experimental yield surfaces reported in the literature for Al 1100 specimen subjected to tensile pre-strain. With the same parameters, the model satisfactorily captures the yield surfaces after torsional pre-strain also. Further:

1. In annealed 1100 Al, two inelastic mechanisms: plasticity and anelasticity, underlie the small-offset yield surface. The experimentally observed yield surface coincides with the inner envelope of the yield surfaces predicted by these mechanisms.The part of yield surface around the forward yield point is governed by plasticity, and that around the reverse yield point by anelasticity.

2. Backstress arising from the substructure are responsible for the sharp curvature of the subsequent yield surfaces near the forward yield point. In the absence of such large backstress, the yield surface would be considerably more rounded near the forward yield point. While coplanar interactions amongst dislocations is principally responsible for the backstress, it is important to also capture the other weaker interactions in order to accurately predict the yield surfaces.
3. Anelastic bowing and unbowing of dislocations are responsible for the large Bauschinger effect observed in the small-offset yield surface. The backstress plays an important supporting role in activating anelastic deformation.

Acknowledgment. Dr. CN Tomé's `POLE7` program was used to compute the pole figures. We thank Prof. SM Keralavarma for valuable discussions and for his comments on this manuscript. We thank M Swamynathan for help with the schematic diagrams.

Declarations

- Funding: The authors did not receive support from any organization for the submitted work.
- Conflict of interest/Competing interests: None
- Ethics approval and consent to participate: Not applicable
- Consent for publication: Not applicable
- Data availability: Not applicable
- Materials availability: Not applicable
- Code availability: On request
- Author contribution: All authors contributed to equally to this work.

References

[1] Mair, W., Pugh, H.L.D.: Effect of pre-strain on yield surfaces in copper. J Mech Eng Sci **6**(2), 150–163 (1964)

[2] Naghdi, P., Essenburg, F., Koff, W.: An experimental study of initial and subsequent yield surfaces in plasticity. J Appl Mech **25**(2), 201–209 (1958)

[3] Ivey, H.: Plastic stress–strain relations and yield surfaces for aluminium alloys. J Mech Eng Sci **3**(1), 15–31 (1961)

[4] Taylor, G., Quinney, H.: The plastic distortion of metals. Phil Trans R Soc London A **230**(681-693), 323–362 (1931)

[5] Phillips, A., Tang, J.-L.: The effect of loading path on the yield surface at elevated temperatures. Int. J. Solids Struct. **8**(4), 463–474 (1972)

[6] Phillips, A., Liu, C., Justusson, J.: An experimental investigation of yield surfaces at elevated temperatures. Acta Mech **14**(2), 119–146 (1972)

[7] Phillips, A., Moon, H.: An experimental investigation concerning yield surfaces and loading surfaces. Acta Mech **27**(1), 91–102 (1977)

[8] Phillips, A., JL, T., Ricciuti, M.: Some new observations on yield surfaces. Acta mechanica **20**, 23–39 (1974)

[9] Stout, M., Martin, P., Helling, D., Canova, G.: Multiaxial yield behavior of 1100 aluminum following various magnitudes of prestrain. Int J Plasticity **1**(2), 163–174 (1985)

[10] Geng, L., Wagoner, R.: Role of plastic anisotropy and its evolution on springback. Int J Mech Sci **44**(1), 123–148 (2002)

[11] Wagoner, R., Lim, H., Lee, M.-G.: Advanced issues in springback. Int J Plasticity **45**, 3–20 (2013)

[12] Yang, H., Zhang, W., Zhuang, X., Zhao, Z.: Phenomenological modeling of deformation-induced anisotropic hardening behaviors: a review. Metals **13**(2), 364 (2023)

[13] Mánik, T.: Independent parameters of orthotropic linear transformation-based yield functions. Mech Mater **190**, 104927 (2024)

[14] Feigenbaum, H., Dafalias, Y.: Directional distortional hardening in metal plasticity within thermodynamics. Int J Solids Struct **44**(22-23), 7526–7542 (2007)

[15] Feigenbaum, H., Dafalias, Y.: Directional distortional hardening at large plastic deformations. Int J Solids Struct **51**(23-24), 3904–3918 (2014)

[16] Barlat, F., Gracio, J., Lee, M.-G., Rauch, E., Vincze, G.: An alternative to kinematic hardening in classical plasticity. Int J Plasticity **27**(9), 1309–1327 (2011)

[17] Mánik, T., Holmedal, B., Hopperstad, O.: Strain-path change induced transients in flow stress, work hardening and r-values in aluminum. Int J Plasticity **69**, 1–20 (2015)

[18] Pietryga, M., Vladimirov, I., Reese, S.: A finite deformation model for evolving flow anisotropy with distortional hardening including experimental validation. Mech Mater **44**, 163–173 (2012)

[19] Liu, F., Fu, Q., Chen, C., Liang, N.: An elasto-plastic damage constitutive theory and its prediction of evolution of subsequent yield surfaces and elastic constants. Int J Plasticity **27**(9), 1355–1383 (2011)

[20] Aria, A., Holmedal, B., Mánik, T., Marthinsen, K.: Crystal-plasticity modelling of the yield surfaces and anelasticity in the elasto-plastic transition of metals. Eur J Mech A, 105417 (2024)

[21] Peeters, B., Seefeldt, M., Teodosiu, C., Kalidindi, S., Houtte, P.V., Aernoudt, E.: Work-hardening/softening behavior of bcc polycrystals during changing strain paths: I. Acta mater **49**, 1607–1619 (2001)

[22] Mahesh, S., Tomé, C., McCabe, R., Kaschner, G., Beyerlein, I., Misra, A.: Application of a sub-structure based hardening model to copper under loading path changes. Metall Mater Trans A **35**, 3763–3774 (2004)

[23] Kitayama, K., Tomé, C., Rauch, E., Gracio, J., Barlat, F.: A crystallographic dislocation model for describing hardening of polycrystals during strain path changes. application to low carbon steels. Int J Plasticity **46**, 54–69 (2013)

[24] Wen, W., Borodachenkova, M., Tomé, C., Vincze, G., Rauch, E., Barlat, F., Grácio, J.: Mechanical behavior of low carbon steel subjected to strain path changes: Experiments and modeling. Acta Mater **111**, 305–314 (2016)

[25] Cormen, T., Leiserson, C., Rivest, R.: Introduction to Algorithms. MIT press, Cambridge (1990)

[26] Mahesh, S.: A hierarchical model for rate-dependent polycrystals. Int J Plasticity **25**(5), 752–767 (2009)

[27] Mahesh, S.: A binary tree based model for rate-independent polycrystals. Int J Plasticity **26**(1), 42–64 (2010)

[28] Honneff, H., Mecking, H.: A method for the determination of the active slip systems and orientation changes during single crystal deformation. In: Proc. 5th Int. Conf. on the Textures of Materials, vol. 1, pp. 265–275. Springer, Berlin (1978)

[29] Khan, A., Pandey, A., Stoughton, T.: Evolution of subsequent yield surfaces and elastic constants with finite plastic deformation. II: A very high work hardening aluminum alloy (annealed 1100 Al). Int J Plasticity **26**(10), 1421–1431 (2010)

[30] Kalidindi, S.R., Bronkhorst, C.A., Anand, L.: Crystallographic texture evolution in bulk deformation processing of FCC metals. J. Mech. Phys. Solids, 537–569 (1992)

[31] Budiansky, B., Wu, T.T.: Theoretical prediction of plastic strains of polycrystals. In: Proceedings of the 4th US National Congress of Applied Mechanics., pp. 1175–1185 (1962)

[32] Lee, Y.-S., Dawson, P.: Obtaining residual stresses in metal forming after neglecting elasticity on loading. Trans ASME J Appl Mech **56**, 318–327 (1989)

[33] Bishop, J.: A theoretical examination of the plastic deformation of crystals by glide. Lond Edinb Dubl Phil Mag **44**(348), 51–64 (1953)

[34] Canova, G., Fressengeas, C., Molinari, A., Kocks, U.: Effect of rate sensitivity on slip system activity and lattice rotation. Acta Metall. **38**(8), 1961–1970 (1988)

[35] Kocks, U., Tomé, C., Wenk, H.: Texture and Anisotropy. Cambridge University Press, Cambridge, U.K. (1998)

[36] Dantzig, G.: Linear Programming and Extensions. Princeton University Press, Princeton, New Jersey (1963)

[37] Chin, G., Mammel, W.: Generalization and equivalence of the minimum work (Taylor) and maximum work (Bishop-Hill) principles of crystal plasticity. Trans. AIME **245**, 1211 (1969)

[38] Makhorin, A.: GNU Linear Programming Kit 5.0. http://www.gnu.org/software/glpk/glpk.html (2020)

[39] Mahesh, S.: Deformation banding and shear banding in single crystals. Acta mater **54**(17), 4565–4574 (2006)

[40] Kocks, U.: Laws for work-hardening and low-temperature creep. ASME J Eng Mater Technol **98**(1), 76–85 (1976)

[41] Rauch, E., Gracio, J., Barlat, F., Vincze, G.: Modelling the plastic behaviour of metals under complex loading conditions. Modelling Simul Mater Sci Eng **19**(3), 035009 (2011)

[42] Franciosi, P., Zaoui, A.: Multislip in FCC crystals: A theoretical approach compared with experimental data. Acta metall **30**, 1627–1637 (1982)

[43] Kubin, L., Devincre, B., Hoc, T.: Modeling dislocation storage rates and mean free paths in face-centered cubic crystals. Acta mater **56**(20), 6040–6049 (2008)

[44] Bay, B., Hansen, N., Kuhlmann-Wilsdorf, D.: Deformation structures in lightly rolled pure aluminum. Mater. Sci Eng A **113**, 385–397 (1989)

[45] Baskaran, R., Akarapu, S., Mesarovic, S., Zbib, H.: Energies and distributions of dislocations in stacked pile-ups. Int J Solids Struct **47**(9), 1144–1153 (2010)

[46] Scardia, L., Peerlings, R., Peletier, M., Geers, M.: Mechanics of dislocation pile-ups: a unification of scaling regimes. J Mech Phys Solids **70**, 42–61 (2014)

[47] Hirth, J., Lothe, J.: Theory of Dislocations. Krieger, Malabar, Florida, USA (1992)

[48] McCabe, R., Misra, A., Mitchell, T.: Experimentally determined content of a geometrically necessary dislocation boundary in copper. Acta mater **52**(3), 705–714 (2004)

[49] Hong, C., Huang, X., Winther, G.: Dislocation content of geometrically necessary boundaries aligned with slip planes in rolled aluminium. Phil Mag **93**(23), 3118–3141 (2013)

[50] Li, D., Wagoner, R.: The nature of yielding and anelasticity in metals. Acta Mater **206**, 116625 (2021)

[51] Leigh, R.: A calculation of the elastic constants of aluminium. The London, Edinburgh, and Dublin Philosophical Magazine and Journal of Science **42**(325), 139–155 (1951)

[52] Ishikawa, H., Sasaki, K.: Yield surfaces of SUS304 under cyclic loading. J Eng Mater Tech **110**(4), 364 (1988)

[53] Sachs, G.: Zur Ableitung einer Fliessbedingung. Z. Ver. Dtsch. Ing. **72**, 734–736 (1928)

[54] Trefethen, L.: Approximation Theory and Approximation Practice. SIAM, Philadelphia (2019)

[55] Liempt, P., Sietsma, J.: A physically based yield criterion I. Mater Sci Eng A **662**, 80–87 (2016)

[56] Meyers, M.A., Ashworth, E.: A model for the effect of grain size on the yield stress of metals. Phil Mag A **46**(5), 737–759 (1982)

[57] Nelder, J., Mead, R.: A simplex method for function minimization. Comput J, 303–313 (1965)

[58] Fletcher, R.A.: Practical Methods of Optimization. Vol 1. Unconstrained Optimization. John Wiley and Sons, ??? (1980)

[59] Hart, E., Solomon, H.: Load relaxation studies of polycrystalline high purity aluminium. Acta Metall **21**(3), 295–307 (1973)

[60] Tomé, C., Canova, G.R., Kocks, U.F., Christodoulou, N., Jonas, J.J.: The relation between macroscopic and microscopic strain hardening in F.C.C polycrystals. Acta metall. **32**(10), 1637–1653 (1984)

[61] Oh, K.: Analysis of texture evolution in fcc metals by full constraint and a self-consistent viscoplastic model. Met Mater **4**, 1127–1131 (1998)

[62] Canova, G., Kocks, U., Jonas, J.: Theory of torsion texture development. Acta Metall **32**(2), 211–226 (1984)

[63] Vallin, J., Mongy, M., Salama, K., Beckman, O.: Elastic constants of aluminum. J Appl Phys **35**(6), 1825–1826 (1964)

[64] Cazzani, A., Rovat, M.: Extrema of Young's modulus for cubic and transversely isotropic solids. Int J Solids Struct **40**(7), 1713–1744 (2003)